Mutations in thyroid hormone receptor α1 cause premature neurogenesis and progenitor cell depletion in human cortical development

Authors:

Teresa G Krieger[a,b,1], Carla M Moran[c], Alberto Frangini[a], W Edward Visser[c2], Erik Schoenmakers[c], Francesco Muntoni[d], Chris A Clark[e], David Gadian[e], Wui K Chong[f], Adam Kuczynski[g], Mehul Dattani[h], Greta Lyons[c], Alexandra Efthymiadou[i], Faraneh Varga-Khadem[g,i], Benjamin D Simons[a,b], Krishna Chatterjee[c], Frederick J Livesey[a,j,3]

Affiliations:

[a] Gurdon Institute, University of Cambridge, Cambridge, UK

[b] Cavendish Laboratory, University of Cambridge, Cambridge, UK

[c] Wellcome Trust-MRC Institute of Metabolic Science, University of Cambridge, Cambridge, UK

[d] Dubowitz Nueromuscular Centre and NIHR Great Ormond St Hospital Biomedical Research Centre or [e]Developmental Imaging and Biophysics Section, or [i]Cognitive Neuroscience and Neuropsychiatry Section, UCL GOS Institute of Child Health, London

Departments of [f]Radiology, [g]Neuropsychology and [h]Endocrinology, Great Ormond St Children's Hospital, London and Genetics and Genomic Medicine Programme, UCL GOS Institute of Child Health, London

[i] Department of Endocrinology, University of Ioannina, 45110 Ioannina, Greece

[j] UCL Great Ormond Street Institute of Child Health, London, UK

[1] Present address: Berlin Institute of Health, Charité BIH CC4, Forum 4, Augustenburger Platz 1, 13353 Berlin, Germany

[2]Erasmus Medical Center, Department of Internal Medicine, Academic Center for Thyroid Diseases, Rotterdam, Netherlands

[3] To whom correspondence may be addressed. Email: r.livesey@ucl.ac.uk

Abstract

Mutations in the thyroid hormone receptor α 1 gene *(THRA)* have recently been identified as a cause of intellectual deficit in humans. Patients present with structural abnormalities including microcephaly, reduced cerebellar volume and decreased axonal density. Here, we show that directed differentiation of *THRA* mutant patient-derived iPSCs to forebrain neural progenitors is markedly reduced, but mutant progenitor cells can generate deep and upper cortical layer neurons and form functional neuronal networks. Quantitative lineage tracing shows that *THRA* mutation-containing progenitor cells exit the cell cycle prematurely, resulting in reduced clonal output. Using a novel micropatterned chip assay, we find that spatial self-organisation of mutation-containing progenitor cells is impaired, consistent with downregulated expression of cell-cell adhesion genes. These results reveal for the first time that thyroid hormone receptor α 1 is required for normal neural progenitor cell proliferation and organisation in human cerebral cortical development. They also exemplify novel quantitative approaches for studying neurodevelopmental disorders using patient-derived cells *in vitro*.

Significance Statement

Thyroid hormone deficiencies are the most common preventable cause of intellectual disability. We report that mutations in the thyroid hormone receptor α1 gene *(THRA)* that result in intellectual disability also reduce brain size. Using human *THRA* mutation stem cell models, we studied the impact of *THRA* mutations on human brain development by combining quantitative lineage analysis, gene expression analyses and novel assays of neuroepithelium formation. We found that *THRA* regulates the balance between progenitor self-renewal and neurogenesis, and thus overall brain size. Importantly, these *in vitro* results are consistent with *in vivo* evidence from MRI imaging of people with these mutations, advancing our understanding of thyroid hormone action in human brain development.

Introduction

The human cerebral cortex mediates higher cognitive and sensorimotor functions, with thyroid hormone deficiency during pregnancy or the neonatal period being recognised as the most common preventable cause of intellectual disability in the world (1). Defects in progenitor cell proliferation, synaptogenesis and dendritic arborisation, neuronal migration and cell survival have been observed in the cerebral cortex of the progeny of hypothyroid rodents (2–4). Aberrant behaviour and cortical cytoarchitecture are observed even following transient thyroid hormone deficiency during the first half of gestation, emphasising the critical role of thyroid hormones for early brain development (5). However, in humans, the actions of thyroid hormones (TH) on cells of the central nervous system (CNS) remain poorly defined (6). In the absence of appropriate *in vitro* models, it has been difficult to study thyroid hormone action in specific cells or tissues, separating its global effects which are likely mediated by a range of tissues and cell types (7).

During cerebral cortex development, thyroid hormones (TH: thyroxine, T4; triiodothyronine, T3) act via a nuclear receptor (TRα1) encoded by the *THRA* gene, to regulate transcription of target genes in a ligand-dependent manner (8–10). Unliganded thyroid hormone receptors (TRs) recruit a corepressor complex to inhibit target gene transcription (11); hormone (T3) occupancy promotes dissociation of the corepressor complex together with coactivator recruitment and transcriptional activation (11, 12).

We reported the first human *THRA* mutation in 2012 (13), and ~29 further patients have since been identified, with shared phenotypic features defining the disorder Resistance to Thyroid Hormone α (RTHα) (14–18). All patients carry heterozygous missense or truncating mutations in the ligand binding domain of TRα1 which disrupt its ability to bind T3, impairing corepressor dissociation and coactivator recruitment (13, 16). When coexpressed, mutant TRα1 inhibits the function of its wild-type counterpart in a dominant-negative manner (13). In addition to growth retardation and skeletal dysplasia, RTHα patients exhibit mild-to-moderate intellectual disability, notably affecting nonverbal IQ and sensorimotor processing, and one adult woman has had epileptic seizures beginning in infancy (16). These findings suggest a crucial role for TRα1 in human cortical neurogenesis, consistent with previous studies reporting a range of CNS abnormalities in mice mutant for TRα1 (19). However, the cellular mechanisms underlying aberrant neural development in RTHα patients are unknown.

Here, we have delineated the neurological and neurocognitive phenotypes and undertaken structural (MRI, tractography) neuroimaging and proton magnetic resonance spectroscopy (MRS) in the first four RTHα patients reported, harbouring frameshift/premature stop *THRA* mutations that are representative of the type of receptor defect found in 50% of the worldwide RTHα cohort (20). We directed differentiation of *THRA* mutant patient-derived iPSCs to a cortical excitatory neuronal fate, using an established *in vitro* system that recapitulates development from early neuroepithelium to functional neuronal circuits (21, 22). Based on quantitative analysis of lineage tracing data, we found that *THRA* mutation-containing cortical progenitor cells are biased towards early differentiation, leading to premature neurogenesis and depletion of the progenitor cell pool. They also exhibit impaired self-organisation into cortical rosette-like structures *in vitro*. Defects in neural progenitor proliferation, cell polarity and apical adhesion may thus contribute to the structural abnormalities and to the sensorimotor and neurocognitive phenotypes seen in RTHα patients.

Results

Neurological, neurocognitive and neuroimaging abnormalities in *THRA* mutation patients

We assessed neurological, neurocognitive and neuroimaging phenotypes in the first four RTHα cases reported (Supplementary Table 1), all harbouring mutations which disrupt the carboxyterminal alpha helix of TRα1 (Fig. 1A). The subjects are a 9 year-old female (E403X TRα1 mutation; referred to as P1 below), a 13 year-old female and her 49 year-old father (F397fs406X TRα1 mutation; P2 and P3), and a 47 year-old female (A382PfsX7 TRα1 mutation; P4). Patients exhibited delayed developmental milestones (Supplementary Table 2) and neurological abnormalities including slow initiation of movement, ataxic gait, dysarthria and fine and gross motor incoordination (Supplementary Table 3).

Neuropsychological examinations showed significantly reduced nonverbal IQ in all cases, with scores ranging from 2 (P1-P3) to 3.4 (P4) standard deviations below the population mean (X=100; SD, 1.5). Furthermore, all patients showed severe impairments in motor coordination, visual motor integration and finger dexterity of both dominant and non-dominant hands. P4 showed intellectual disability affecting verbal as well as nonverbal abilities, whereas verbal abilities were relatively preserved in P1-P3. Performance on a test of visual perception was within the low average to average range in P1-P3 (Supplementary Table 4).

MRI scans revealed reduced cerebellar volumes in all four patients (Fig. 1B), with microencephaly in the adult cases (P3, P4), despite their increased skull volume (macrocephaly) (Fig. 1C). Diffusion Tensor Imaging (DTI), undertaken in P1 and P2, showed a global increase in mean diffusivity (MD) of water in white matter tracts, denoting a reduction in their density (Fig. 1D). On MRS, there was a reduced ratio of N-acetylaspartate (NAA) to creatine plus phosphocreatine (Cr) ratio in the frontal white matter and thalamus of patients, suggestive of neuronal loss or dysfunction (P2, P3, P4) (Supplementary Table 5). These results suggest that the observed neurocognitive and sensorimotor deficits in the patients are related to structural abnormalities in several brain regions, including the cerebellum and cerebral cortex.

Reduced differentiation of *THRA* mutant iPSCs to forebrain neuroepithelial cells

To study the cellular developmental origin of cortical abnormalities in *THRA* mutant patients, iPSC lines were derived from P1, P2 and P4 by reprogramming with non-integrating Sendai virus (Supplementary Fig. 1A) (23). *THRA* mutant and control iPSCs were then differentiated

to cerebral cortex neural progenitor cells using an established protocol based on dual SMAD inhibition (Fig. 2A) (21, 22). After 12 days of induction, a neuroepithelial sheet was formed in control cultures, and expression of PAX6 and FOXG1 mRNA confirmed cortical identity (Supplementary Fig. 1B,C). Neural progenitor cells proceeded to generate neurons as described previously (22). In control cultures, TRα1 was expressed in stem cells prior to cortical induction, in cycling (Ki67^{+}) progenitor cells, and in postmitotic (Tuj1^{+}) neurons (Fig. 2B and Supplementary Fig. 1D), confirming that the receptor is present throughout the *in vitro* differentiation process.

When *THRA* mutation-containing iPSCs from the three patients were subjected to the same differentiation protocol, cortical induction was found to be reduced in efficiency. While cortical transcription factors were also expressed in *THRA* mutant cultures (Supplementary Fig. 1B), expression of PAX6 was highly variable between cells (Supplementary Fig. 1C). At day 15, following manual fragmentation of the neuroepithelial sheet, PAX6 expression in *THRA* mutation-containing cells was decreased (Fig. 2C).

Altered expression of neural development and cell-cell adhesion genes during neural differentiation of *THRA* mutant iPSCs

To investigate differences in induction efficiency in an unbiased manner, we performed RNA sequencing of three independent neural inductions from each THRA mutation-containing iPSC line (TRα1-403X carrying the E403X mutation, TRα1-FS382 with the A382PfsX7 mutation, and TRα1-FS397 with the F397fs406X mutation) and one neural induction from each control line (H9, NAS6 and NDC), at day 12 of cortical induction. Out of 16,773 transcripts that were detected above negligible levels in all samples, we considered 478 transcripts whose expression differed significantly between *THRA* mutation-containing and control lines (FDR<0.25, independent of the sign of the fold change).

Hierarchical clustering analysis revealed that the expression profiles of replicate inductions from each *THRA* mutation-containing line clustered together, suggesting that the cortical induction process *in vitro* preserves mutation-specific differences in transcription (Fig. 3A). The differentially expressed genes clustered into four distinct groups, with the largest subset representing genes whose expression is downregulated in THRA mutation-containing versus control cells, consistent with the known repressive function of TRα1 (209 genes in group C). Gene Ontology (GO) analysis showed that many of these downregulated genes relate to DNA-templated transcription, ectoderm and nervous system development, or cell-cell adhesion via

membrane adhesion molecules (Supplementary Table and Figure 3B), with substantial overlap (Figure 3C). Genes relating to both transcription and neural development include bHLH-transcription factors such as *NEUROD1*, *NEUROD4* (*MATH3*) and *NEUROG2*, which are involved in normal cerebral cortex development (24), as well as *LHX2*, known to regulate the specification of cortical regional fates (25). The genes involved in both neural development and cell-cell adhesion are six protocadherins (part of the cadherin family), the autism susceptibility gene *NRXN1* (neurexin), and *NPTN* (neuroplastin), which has been associated with cortical thickness and intellectual ability in humans (26, 27).

Thus, our RNA-seq data show that *THRA* mutations are associated with globally decreased transcription and downregulation of genes involved in neural development. In addition, the data suggest that cell-cell adhesion in *THRA* mutation-containing cells is compromised, possibly contributing to impaired cortical growth. Notably, within upregulated (group B) genes, enrichment for non-neural differentiation fates was not detected, suggesting that reduced efficiency of neural induction seen in *THRA* mutation-containing cells is not due to differentiation down non-neural paths.

CD271⁻CD44⁻ cortical progenitor cells generate functional neurons *in vitro*

To compare neural development from *THRA* mutation-containing versus control cortical progenitors whilst controlling for differences in induction efficiency, cultures were enriched for neural stem cells by FACS at day 16 post neural induction. Based on an established neural stem cell signature (28), the CD271⁻CD44⁻ population was isolated and propagated (Fig. 4A). CD271 is expressed in neural crest precursors (29, 30), which are occasionally observed as a contaminant in control cortical inductions *in vitro*, and were identified based on their characteristic morphology to be more prominent in *THRA* mutant inductions. Negative selection for CD44, a pluripotent stem cell marker (28), eliminated cells that had failed induction to neural stem cell fate. Depending on induction efficiency, ~50-80% of induced *THRA* mutation-containing cells were FACS-selected for propagation (Fig. 4A). FACS-enriched cultures expressed PAX6 and the intermediate filament protein vimentin (VIM), both neural progenitor cell markers (Fig. 4A).

Over time, FACS-sorted progenitors gave rise to neurons expressing the transcription factors TBR1 and CTIP2, expressed by deep cortical layer neurons (Fig. 4B). Most neurons also showed punctate vesicular glutamate transporter (VGLUT1) expression, indicating their glutamatergic identity (Fig. 4B). Overall, FACS successfully enriched for cortical neural

progenitors derived from *THRA* mutation-containing iPSCs, which proceeded to generate cortical excitatory neurons over time *in vitro*.

To assess neuronal function, 60 day old *THRA* mutation-containing and control cultures were analysed by single-cell electrophysiology. *THRA* mutation-containing neurons fired action potentials normally in response to stepwise current injections (Fig. 4C) and displayed sodium and potassium currents in response to voltage stimulation (Supplementary Fig. 2A). Spontaneous miniEPSCs were observed in a similar proportion of *THRA* mutation-containing and control neurons (Supplementary Fig. 2A). *THRA* mutation-containing neurons appeared significantly more mature than controls, with a greater proportion of cells firing action potentials (10/11 in FS397 compared to in 8/14 in H9), more action potentials fired in the average burst, larger mean peak sodium and potassium currents, and a lower average membrane potential (-54 ± 2 mV in FS397; -48 ± 3 mV in H9). These differences might represent variation in individual neuronal properties, but could also be due to earlier production of neurons in *THRA* mutation-containing cultures.

By day 50 post induction, both control and *THRA* mutation-containing cells developed spontaneous neuronal network activity, visualized by calcium imaging (Fig. 4D and Supplementary Fig. 2B). Spontaneous activity was blocked by the sodium channel blocker tetrodotoxin (TTX) and substantially reduced by the AMPA receptor antagonist CNQX, indicating that a significant element of the observed spontaneous neuronal activity is mediated by excitatory synaptic transmission (Supplementary Fig. 2C).

Compromised cortical progenitor cell dynamics in *THRA* mutation-containing cells

Microcephaly and reduced white matter tract density seen in RTHα patients suggested that structural differences in the cerebral cortex might contribute to their neurocognitive phenotype. With human cortex comprising columns of clonally-related excitatory neurons preferentially synapsing with each other (31), the clonal output of a cortical progenitor cell is a major contributor to cortical size, architecture, and function. To determine whether defects in early cortical development could contribute to the neurological phenotypes of patients, we undertook single-cell clonal lineage analysis of cortical progenitors, comparing cell dynamics and clonal output of *THRA* mutation-containing versus control cells. A small proportion (≤1%) of *THRA* mutation-contaning or control cortical progenitor cells, infected with a GFP-expressing replication-incompetent lentivirus, were mixed with unlabelled control cultures at day 30 and day 40 post cortical induction. Their progeny was then traced over time, enabling the

delineation of cell-intrinsic differences between *THRA* mutation-containing and control progenitor cells (Fig. 5A).

The size and composition of clones (2 or more cells) derived from labelled progenitors were analysed at 2, 6 and 10 days after mixing. The majority of labelled cells expressed either Ki67 or the neuron-specific marker βIII-tubulin, indicating that clones consisted of cycling progenitors and neurons (Fig. 5B). Across the three *THRA* mutation-containing and three control cell lines (hiPSC lines NDC and NAS6, and hESC line H9), the average size of clones increased progressively over the 10-day period after labelling (Fig. 5C). Average clone sizes were similar in control cortical progenitor cells labelled at either day 30 or day 40, whereas the size of *THRA* mutation-containing clones labelled at day 40 was markedly reduced.

Analysing clone composition, the average number of progenitor cells per clone (as assessed by Ki67 expression) increased in control cultures at day 30 and 40 (Fig. 5C). In *THRA* mutation-containing cultures, progenitor cell numbers increased only slightly at day 30 and decreased at day 40, suggesting a differing pattern of cell division with earlier cell cycle exit of *THRA* mutation-containing progenitors. Thus, depletion of the THRA mutation-containing progenitor pool leads to premature neuron production and a decrease in clonal output over time. By live imaging of cells over a 48-hour period, we confirmed that these differences were not due to altered cell cycle kinetics or increased cell death (Supplementary Fig. 3).

Premature cell cycle exit of *THRA* mutation-containing cortical progenitor cells
To further quantitate the division pattern of progenitor cells, fully differentiated clones were distinguished from persisting clones containing at least one progenitor cell (Fig. 6A). The proportion of persisting clones decreased more rapidly in *THRA* mutation-containing than control cultures (Fig. 6A). At the same time, the average size of persisting clones increased near-exponentially in control but more linearly in *THRA* mutant cells at day 40 (Fig. 6B), suggesting that a higher proportion of control progenitor cells are self-renewing symmetrically, whereas *THRA* mutation-containing progenitor cells have transitioned to a more asymmetric, neurogenic division pattern.

To test this, we developed a computational model of human cortical development in which symmetrically or asymmetrically self-renewing radial glia (RGs) produce intermediate progenitor cells (IPCs), which generate neurons through asymmetric or terminal divisions (Supplementary Methods and Supplementary Fig. 4). We found that this model could largely

account for differences in clonal behaviour of *THRA* mutation-containing versus control cells, including the distribution of clone size and composition, under the single assumption that the fate choice of *THRA* mutation-containing RGs was tilted towards differentiation into IPCs (Fig. 6B,C). Therefore, the clonal lineage data and the computational model together demonstrate that *THRA* mutation-containing progenitors switch to neurogenesis earlier than control cells, which continue proliferating.

Cell polarity and rosette self-assembly defects in *THRA* mutation-containing cortical progenitor cells

Previous studies have shown that cortical progenitor cell polarity and attachment at the ventricular surface maintain progenitor identity and proliferation in the mouse cortex (32), consistent with our gene expression data above. The functional units of corticogenesis in the *in vitro* system are rosette-like arrangements of progenitor cells, which self-assemble and recreate aspects of the *in vivo* niche (22). We observed that following dissociation, *THRA* mutation-containing progenitors self-organised into rosettes less readily than controls. To quantify the efficiency of rosette formation, progenitor cells were plated at a defined density onto micropatterned chips that only allow cell adhesion in circular areas of different diameters (Fig. 7A).

In control lines, rosettes formed efficiently within 48 hours after plating, with areas of 140 μm diameter predominantly hosting a single rosette (Fig. 7B). The organisation of cell types within rosettes showed clear apical-basal polarity (Fig. 7C). In contrast, rosette formation was substantially impaired in *THRA* mutation-containing cell cultures (Fig. 7D). Treatment of control cultures with the competitive thyroid hormone receptor antagonist 1-850 (33) decreased rosette formation efficiency and proliferation, confirming that the impairment was due to aberrant thyroid signalling (Supplementary Fig. 5A).

The mechanisms underlying neural rosette formation *in vitro* are largely enigmatic (34). Live imaging of control cultures for up to 72 hours after plating found no evidence for directional movement of cells, suggesting that cells do not respond to chemotactic signals (Supplementary Fig. 5B). To test which factors are required for rosette formation, we developed a computational model in which cells move randomly and form attachments at their apical ends when in close proximity. Both the number of rosettes and the distribution of rosette centres observed *in vitro* were statistically reproduced *in silico*, indicating that migration and apical attachment are sufficient for rosette formation (Supplementary Fig. 5C). As migration defects were not

apparent from the live-imaging data (Supplementary Fig. 5B), impaired apical attachments may be limiting rosette formation efficiency in *THRA* mutation-containing cultures.

In support of this notion, N-cadherin was highly localised to the apical end of progenitor cells in control rosettes but expressed along the cell membrane in *THRA* mutation-containing cells, suggesting impaired adherens junction formation (Fig. 7D and Supplementary Fig. 5D), consistent with the downregulation of protocadherins observed by RNA-seq. Apical expression of the polarity complex protein PKCζ and the centrosome-associated γ-tubulin was observed in control progenitor but not in *THRA* mutation-containing cells (Supplementary Fig. 5D). Defects in progenitor cell polarity and spatial organisation may thus contribute to their premature cell cycle exit.

Discussion

Consistent with the known critical role of thyroid hormone in brain development, we have documented neurocognitive deficits (reduced nonverbal IQ, motor incoordination, impaired visual motor integration) in RTHα patients, with some deficits (e.g. motor incoordination, poor finger/hand dexterity) resembling consequences of untreated congenital hypothyroidism. Structural abnormalities include reduction in cerebellar volume, cortical microcephaly in adult cases and decreased white matter tract density. The neurocognitive, structural and functional deficits observed in RTHα patients suggested abnormalities in several brain regions, including the axis from the cerebellum to the neostriatum and the cerebral cortex.

Accordingly, we studied cortical neural progenitors derived from *THRA* mutation-containing iPSCs from these patients, enabling *in vitro* ascertainment of the effects of mutant TRα1 on human cortical neurogenesis and function. We found that *THRA* mutation-containing cortical progenitor cells differentiate prematurely *in vitro*, with attendant depletion of the progenitor cell pool reducing clonal output, which *in vivo* would result in microcephaly. Quantitative analysis of lineage tracing data confirmed that the fate choices of *THRA* mutation-containing cortical progenitor cells are biased towards neuronal differentiation as opposed to the continued self-renewal observed in control cells. As single labelled *THRA* mutation-containing progenitor cells were studied in wild-type background cultures, such alterations in clonal dynamics likely reflect distinct cell-autonomous fate behaviours.

RNA sequencing of early cortical progenitors revealed downregulated expression of genes involved in cell polarity or adherence in *THRA* mutation-containing cortical progenitor cells. Consistently, we found defective self-organisation of these cells into rosettes. In rodent studies, ventricular attachment through adherens junctions is intimately linked to apical-basal polarity and self-renewal of radial glia (32, 35). Defects in cell polarity and attachment to neighbouring stem cells may thus mediate the premature cell cycle exit observed in *THRA* mutation-containing cortical progenitor cells. These findings also suggest that some cell-intrinsic consequences of mutant TRα1 dysfunction may only become apparent through interactions with the local niche. Whether cortical neuronal differentiation is initiated by apical detachment, the loss of cell polarity, or upstream transcriptional changes, remains unclear. Future studies may establish the functional hierarchy of determinants of cortical progenitor identity, to further delineate mechanisms whereby mutant TRα1 affects neurogenesis.

Overall, we suggest that abnormal proliferation, adhesion and organization of *THRA* mutation-containing cortical neural progenitors forms the basis, at least in part, of structural and functional changes culminating in neurocognitive deficits seen in RTHα patients.

Reduced cortical progenitor output and impaired cortical architecture have been observed in human patients and mouse models of several other neurodevelopmental disorders, including Down's syndrome, schizophrenia, and autism spectrum disorders (36–39). A number of genes differentially expressed in *THRA* mutation-containing cells, including the cell-surface dystroglycan receptor *NRXN1* (neurexin) and the transmembrane protein *NPTN* (neuroplastin), have also been implicated in other neurodevelopmental disorders (26, 27). Since normal cortical progenitor self-renewal requires the orchestration of a range of cell-intrinsic and environmental factors, including transcription factors determining cortical stem cell identity and genes regulating cell attachment, proliferation and movement, cytoskeletal organisation and polarity (32), a range of gene defects may converge onto similar abnormal neurodevelopmental phenotypes. Specifically, our observations suggest that impaired cell adhesion, leading to defective cortical size and architecture, may ultimately result in neurocognitive deficits across a range of genetic disorders.

In addition to mouse models, novel human iPSC-derived *in vitro* systems are increasingly used to study neurodevelopmental conditions, hitherto focusing on neuronal maturation and network function (40–44). Extending these approaches, this study describes a method to assess the proliferative potential and fate of neural stem cells *in vitro*. Through quantitative analysis of lineage tracing data, even minor differences in clonal dynamics can be resolved. In addition, we have developed a novel quantitative assay for the self-organising capacity of neural stem cells. Together, these approaches provide an experimental platform to investigate the function of cortical progenitor cells with differing genetic backgrounds, study neural progenitor cell dynamics during normal and pathological development, and ultimately screen for agents to ameliorate defective neurogenesis.

References

1. Bath SC, Steer CD, Golding J, Emmett P, Rayman MP (2013) Effect of inadequate iodine status in UK pregnant women on cognitive outcomes in their children: Results from the Avon Longitudinal Study of Parents and Children (ALSPAC). *Lancet* 382(9889):331–337.

2. Mohan V, et al. (2012) Maternal thyroid hormone deficiency affects the fetal neocorticogenesis by reducing the proliferating pool, rate of neurogenesis and indirect neurogenesis. *Exp Neurol* 237(2):477–88.

3. Pathak A, Sinha RA, Mohan V, Mitra K, Godbole MM (2011) Maternal thyroid hormone before the onset of fetal thyroid function regulates reelin and downstream signaling cascade affecting neocortical neuronal migration. *Cereb Cortex* 21(1):11–21.

4. Lavado-Autric R, et al. (2003) Early maternal hypothyroxinemia alters histogenesis and cerebral cortex cytoarchitecture of the progeny. *J Clin Invest* 111(7):1073–1082.

5. Ausó E, et al. (2004) A moderate and transient deficiency of maternal thyroid function at the beginning of fetal neocorticogenesis alters neuronal migration. *Endocrinology* 145(9):4037–47.

6. Moog NK, et al. (2017) Influence of maternal thyroid hormones during gestation on fetal brain development. *Neuroscience* 342:68–100.

7. Horn S, Heuer H (2010) Thyroid hormone action during brain development: more questions than answers. *Mol Cell Endocrinol* 315(1–2):19–26.

8. Bernal J (2007) Thyroid hormone receptors in brain development and function. *Nat Clin Pract Endocrinol Metab* 3(3):249–59.

9. Vaquerizas JM, Kummerfeld SK, Teichmann SA, Luscombe NM (2009) A census of human transcription factors: Function, expression and evolution. *Nat Rev Genet* 10(4):252–263.

10. Bradley DJ, Towle HC, Young WS (1992) Spatial and temporal expression of alpha- and beta-thyroid hormone receptor mRNAs, including the beta 2-subtype, in the developing mammalian nervous system. *J Neurosci* 12(6):2288–2302.

11. Astapova I, et al. (2008) The nuclear corepressor, NCoR, regulates thyroid hormone action in vivo. *Proc Natl Acad Sci* 105(49):19544–19549.

12. Ito M, Yuan CX, Okano HJ, Darnell RB, Roeder RG (2000) Involvement of the

TRAP220 component of the TRAP/SMCC coactivator complex in embryonic development and thyroid hormone action. *Mol Cell* 5(4):683–693.

13. Bochukova E, et al. (2012) A mutation in the thyroid hormone receptor alpha gene. *N Engl J Med* 366(3):243–9.

14. van Mullem A, et al. (2012) Clinical phenotype and mutant TRα1. *N Engl J Med* 366:201–204.

15. Moran C, et al. (2014) Resistance to thyroid hormone caused by a mutation in thyroid hormone receptor (TR)α1 and TRα2: clinical, biochemical, and genetic analyses of three related patients. *Lancet Diabetes Endocrinol*:619–626.

16. Moran C, et al. (2013) An adult female with resistance to thyroid hormone mediated by defective thyroid hormone receptor α. *J Clin Endocrinol Metab* 98(November 2013):4254–61.

17. Espiard S, et al. (2015) A novel mutation in THRA gene associated with an atypical phenotype of resistance to thyroid hormone. *J Clin Endocrinol Metab* 100(8):2841–2848.

18. Tylki-Szymanska A, et al. (2015) Thyroid hormone resistance syndrome due to mutations in the thyroid hormone receptor α gene (THRA). *J Med Genet* 52(5):312–316.

19. Fauquier T, et al. (2011) Severe impairment of cerebellum development in mice expressing a dominant-negative mutation inactivating thyroid hormone receptor alpha1 isoform. *Dev Biol* 356(2):350–8.

20. Moran C, Chatterjee K (2016) Resistance to thyroid hormone α-emerging definition of a disorder of thyroid hormone action. *J Clin Endocrinol Metab* 101(7):2636–2639.

21. Shi Y, Kirwan P, Livesey FJ (2012) Directed differentiation of human pluripotent stem cells to cerebral cortex neurons and neural networks. *Nat Protoc* 7(10):1836–46.

22. Shi Y, Kirwan P, Smith J, Robinson HPC, Livesey FJ (2012) Human cerebral cortex development from pluripotent stem cells to functional excitatory synapses. *Nat Neurosci* 15(3):477–86.

23. Park I-H, et al. (2008) Disease-specific induced pluripotent stem cells. *Cell* 134(5):877–886.

24. Johnson MB, et al. (2015) Single-cell analysis reveals transcriptional heterogeneity of neural progenitors in human cortex. *Nat Neurosci* 18(5):637–646.

25. Chou SJ, Perez-Garcia CG, Kroll TT, O'Leary DDM (2009) Lhx2 specifies regional

fate in Emx1 lineage of telencephalic progenitors generating cerebral cortex. *Nat Neurosci* 12(11):1381–1389.

26. Kim H-G, et al. (2008) Disruption of neurexin 1 associated with autism spectrum disorder. *Am J Hum Genet* 82(January):199–207.

27. Desrivières S, et al. (2015) Single nucleotide polymorphism in the neuroplastin locus associates with cortical thickness and intellectual ability in adolescents. *Mol Psychiatry* 20(2):263–274.

28. Yuan SH, et al. (2011) Cell-surface marker signatures for the isolation of neural stem cells, glia and neurons derived from human pluripotent stem cells. *PLoS One* 6(3):e17540.

29. Lee G, et al. (2007) Isolation and directed differentiation of neural crest stem cells derived from human embryonic stem cells. *Nat Biotechnol* 25(12):1468–1475.

30. Morrison SJ, White PM, Zock C, Anderson DJ (1999) Prospective identification, isolation by flow cytometry, and in vivo self-renewal of multipotent mammalian neural crest stem cells. *Cell* 96(5):737–749.

31. Yu Y-C, Bultje RS, Wang X, Shi S-H (2009) Specific synapses develop preferentially among sister excitatory neurons in the neocortex. *Nature* 458(7237):501–4.

32. Götz M, Huttner WB (2005) The cell biology of neurogenesis. *Nat Rev Mol Cell Biol* 6(10):777–788.

33. Schapira M, et al. (2003) Discovery of diverse thyroid hormone receptor antagonists by high-throughput docking. *Proc Natl Acad Sci U S A* 100(12):7354–7359.

34. Karus M, Blaess S, Brüstle O (2014) Self-organization of neural tissue architectures from pluripotent stem cells. *J Comp Neurol* 522(12):2831–44.

35. Kosodo Y, et al. (2004) Asymmetric distribution of the apical plasma membrane during neurogenic divisions of mammalian neuroepithelial cells. *EMBO J* 23(11):2314–2324.

36. Chakrabarti L, Galdzicki Z, Haydar TF (2007) Defects in embryonic neurogenesis and initial synapse formation in the forebrain of the Ts65Dn mouse model of Down syndrome. *J Neurosci* 27(43):11483–95.

37. Meechan DW, Tucker ES, Maynard TM, LaMantia A-S (2009) Diminished dosage of 22q11 genes disrupts neurogenesis and cortical development in a mouse model of 22q11 deletion/DiGeorge syndrome. *Proc Natl Acad Sci* 106(38):16434–16445.

38. Gallagher D, et al. (2015) Ankrd11 is a chromatin regulator involved in autism that is

essential for neural development. *Dev Cell* 32(1):31–42.

39. LaMonica BE, Lui JH, Wang X, Kriegstein AR (2012) OSVZ progenitors in the human cortex: An updated perspective on neurodevelopmental disease. *Curr Opin Neurobiol* 22(5):747–753.

40. Brennand KJ, et al. (2011) Modelling schizophrenia using human induced pluripotent stem cells. *Nature* 473(7346):221–5.

41. Paşca SP, et al. (2011) Using iPSC-derived neurons to uncover cellular phenotypes associated with Timothy syndrome. *Nat Med* 17(12):1657–1662.

42. Chamberlain SJ, et al. (2010) Induced pluripotent stem cell models of the genomic imprinting disorders Angelman and Prader – Willi syndromes. *Pnas* 107(41):17668–17673.

43. Marchetto MCN, et al. (2010) A model for neural development and treatment of Rett syndrome using human induced pluripotent stem cells. *Cell* 143(4):527–39.

44. Muotri AR, et al. (2010) L1 retrotransposition in neurons is modulated by MeCP2. *Nature* 468(7322):443–446.

Acknowledgements

Author contributions

T.G.K. C.M, K.C and F.J.L. designed the study. T.G.K. performed *in vitro* experiments, data analysis and computational modelling, and wrote the paper. E.S. generated patient-derived iPSC lines. C.M., E.V, F.M, C.C, D.G, Kl.C, A.K, M.D, F.V-K and K.C. contributed neurocognitive and neuroimaging data. A.F. prepared RNA-seq libraries. B.D.S. advised on the computational modelling. All authors commented on the manuscript.

Methods

Neuroimaging

Whole brain MRI scanning was performed on a 1.5T Siemens Magnetom Avanto Scanner (Siemens, Erlangen, Germany) at Great Ormond Street Hospital, London, UK. Axial T2 weighted fluid attenuated inversion recovery (FLAIR) images and coronal T1 weighted scans were compared with healthy age-matched controls. Diffusion Tensor Imaging was performed as described previously (45), and results compared with data from 20 age and gender-matched controls.

Proton magnetic resonance spectra (acquired using a point-resolved spectroscopy (PRESS) sequence with TR=1600ms, TE=135ms and a voxel size of 2 x 2 cm) of frontal white matter and thalamus of patients were analysed for N-acetylaspartate (NAA) and creatine plus phosphocreatine (Cr), with the results expressed as a ratio (NAA/Cr) and compared to a reference range from healthy, age-matched control subjects (46–50).

Pluripotent stem cell culture and directed cortical differentiation

Human control PSCs (H9 ESCs,WiCell Research Institute; NDC1.2 iPSCs (Israel et al., 2012); NAS6 iPSCs (T. Kunath, Edinburgh) and *THRA* mutant iPSCs were cultured under feeder-free conditions in Essential 8 Medium on Geltrex-coated tissue culture plates (Life Technologies). Neural induction was performed as previously described (Shi et al., 2012b). Briefly, confluent PSCs were incubated for 12 days with a 1:1 mixture of N2 and B27 medium supplemented with 100 nM LDN-193189 (Stemgent) and 10μM SB431542 (Tocris). The neuroepithelial sheet was then broken up with Dispase (Life Technologies), and plated onto laminin-coated plates with N2B27 medium supplemented with 20 ng/ml FGF2 (Peprotech) for 4 days. From day 16 of induction, cells were maintained in N2B27 medium up to 60 days.

FACS sorting

Cells were dissociated with Accutase (Sigma-Aldrich, cat. no. A6964) for 10 minutes at 37°C with triturating every 5 minutes. Following incubation in DNaseI at 100 units/ml for 10 minutes, cells were strained through a 50μm cell strainer and counted. For each sample, 10^6 cells were collected by centrifugation and stained with fluorochrome-conjugated antibodies (BD Biosciences) in 100 μl neural maintenance medium containing 0.5% FBS (Hyclone, Fisher Scientific, cat. no. 12359792) and 0.5 mM EDTA (Life Technologies, cat. no. 15575-020) for 30 minutes on ice. Stained cells were sorted using an S3 Cell Sorter (Bio-Rad) in N2B27 medium with 10 μM ROCK inhibitor Y-27632 dihydrochloride (Tocris, cat. no. 1254).

RT-PCR

Total RNA from cortical cultures was isolated using Trizol (Sigma), and reverse-transcribed to cDNA using random hexamer primers (Applied Biosciences). Semi-quantitative RT-PCR was performed using primers against *FOXG1*, *PAX6* and *GAPDH*, and visualized in a Gel Doc XR+ Imager (Biorad).

Western blotting

Protein was extracted from overnight frozen cell pellets at -80°C, using Cell Extraction Buffer (Invitrogen) containing 1x complete mini protease inhibitor (Thermo Scientific). The insoluble fraction was removed by centrifugation at 12,000 g for 15 min at 4°C. Protein concentration was determined using Precision Red Advanced Protein Assay (Cytoskeleton, Inc.) according to manufacturer's instructions. 10-30 µg of total protein were mixed with NuPAGE LDS Sample Buffer and NuPAGE Reducing Agent to a final concentration of 1x. Samples were heated to 95°C for 10 min and cooled on ice prior to loading on pre-cast Bis-Tris gels and run at 200 V for at least 1 h. Proteins were transferred from the gel onto pre-soaked LiCOR PVDF membranes for 1h at 100V in 1x Tris-Glycine buffer with 20% methanol. Following transfer, the membrane was washed in TBS with 0.1% Tween (TBST), then blocked for 1 h at room temperature in TBST and 3% BSA (TBST+B). Membranes were incubated with β-actin and TRα1 (Pierce, cat. no. PA1-211A) primary antibodies diluted in TBST+B overnight at 4°C. The membrane was then washed five times with TBST and incubated in secondary antibody diluted 1:5,000 in TBST+B for 2 h at room temperature. Following a further five washes in TBST, the membrane was visualised on an Odyssey LiCOR machine. Band intensity was measured using Image Studio software (Li-COR), and normalised to β-actin.

Electrophysiology

For electrophysiological recordings, cortical neurons were incubated with artificial cerebral spinal fluid (aCSF) containing 125mM NaCl, 25mM $NaHCO_3$, 1.25mM NaH_2PO_4, 3mM KCl, 2mM $CaCl_2$, 25mM glucose and 3mM pyruvic acid, equilibrated in 95% O_2 and 5% CO_2. Borosilicate glass electrodes with resistance of 6-10MΩ were filled with an artificial intracellular solution, containing 135mM potassium gluconate, 7mM NaCl, 10mM HEPES, 2mM Na_2ATP, 0.3mM Na_2GTP and 2mM $MgCl_2$, and positioned over a cortical neuron to form a whole-cell patch. Recordings were made using a Multiclamp 700A amplifier (Molecular Devices), and signals were sampled and filtered at 20kHz and 6kHz respectively. A low-pass Gaussian filter was applied to filter out high frequency noise. To detect sodium and potassium currents, step depolarisations were applied from a holding potential of -80 mV up to +40 mV

in voltage clamp mode. To detect action potentials, stepwise current injections were applied from -10 pA up to +60 pA in steps of 5-10 pA in current clamp mode. To measure miniEPSCs, cells were held at -70 mV and current was recorded for 2-5 min.

Calcium imaging

Cells were incubated in N2B27 medium containing 3.2 µM calcium indicator Oregon Green 488 BAPTA and 0.01% v/v Cremaphor EL for 1 h at 37°C with 7% CO_2 in the dark. Cells were then incubated in N2B27 medium for a further 30 min at 37°C with 7% CO_2 in the dark. Neural maintenance medium was replaced with aCSF before imaging, and cells were placed in a microscope chamber heated to 37°C with 5% CO_2. Calcium activity in cultures was recorded at 10 Hz on a Deltavision fluorescence microscope with an EMCCD camera (Applied Precision) and using softWoRx 5.0.0 software. Three to five two-minute videos were recorded from one to two independent inductions from each cell line. For pharmacological experiments, cells were incubated in aCSF containing 50µM CNQX (Tocris Bioscience, cat. no. 0190) or 1µM tedrodotoxin (Tocris Bioscience, cat. no. 1078). Cells were imaged 10 min after drug application and 10 min after washout.

Movies were created from individual image files using ImageJ, and analysed with custom written software (based on templates written by Hugh Robinson, PDN, Cambridge) in Matlab (MathWorks). To quantify the level of calcium activity, the total calcium activity A_{Ca} was calculated as the change in fluorescent signal (ΔF/F) integrated over time, as

$$A_{Ca} = \int_{t} \left| \frac{d}{dt} \Delta F/F \right|.$$

Results from 3-5 videos per induction were averaged.

Immunofluorescence and imaging

For immunocytochemistry, cells were fixed with 4% paraformaldehyde in PBS and processed for immunofluorescence staining. Primary antibodies used: α-acetylated α tubulin (Sigma-Aldrich T6793), α-atypical PKC (Santa Cruz sc-216), α-βIII tubulin (Covance PRB-435P), α-cleaved Caspase 3 (Cell Signaling 9661L), α-Ctip2 (Abcam ab18465), α-γ-tubulin (Abcam ab11316), α-Ki67 (BD 550609), α-MAP2 (Abcam ab5392), α-Nanog (R&D Systems AF1997), α-N-cadherin (Abcam ab18203), α-Nestin (Abcam ab22035), α-Oct4 (Abcam ab19857), α-PAX6 (Covance PRB-278P), α-phospho-histone H3 (Abcam ab10543), α-SATB2 (Abcam ab51502), α-SSEA4 (Santa Cruz sc-21704), α-TBR1 (Abcam ab31940), α-TRα1 (Pierce PA1-211A), α-Tra-1-60 (Abcam ab16288), α-Vimentin (Abcam ab8973), α-vGlut1 (Synaptic systems 135 303). Immunostained samples were imaged using a Leica SP5 inverted confocal microscope.

Clonal lineage analysis

Third generation replication-incompetent lentivirus was produced by calcium phosphate transfection of HEK293T cells, using pBOP-GFP plasmids combined with packaging plasmids pRSV-Rev, pMDLg/pRRE and pMD2.G. For clonal lineage analysis, cortical progenitor cells were infected with the lentivirus at high titre before isolation of the CD271⁻CD44⁻ population by FACS. At day 30 and day 40, sorted progenitors were mixed with unlabeled controls cultures and plated at a density of $1.0x10^5$ cells/cm². Cultures were fixed and immunostained at 2, 6 and 10 days after plating.

Micropattern chip cultures

Neural progenitor cells were dissociated using Accutase, washed once in N2B27 and strained through a 50 μm cell strainer before counting. 10^6 cells were plated onto laminin-coated CYTOOchips in neural maintenance medium containing 20 ng/ml FGF2. After 24 hours, the medium was replaced with neural maintenance medium without FGF2, and cultures were kept for 1-7 days.

Live imaging

For live imaging, tissue culture dishes containing cells in N2B27 medium were placed in a BioStation CT (Nikon) at 37°C with 7% CO_2. Images were acquired in phase and green fluorescence channels at 10x or 20x magnification every 10 minutes for a period of 48-72 hours.

RNA sequencing

For RNA-seq library preparation, total RNA was extracted (as outlined above) from 3 control lines (H9, NDC1.2 and NAS6, 1 induction per line) and 3 *THRA* mutant lines (P1, P2 and P4, 3 independent inductions per line), all at day 12 of *in-vitro* cortical induction. A total of 2 μg of RNA were purified and in-column DNase-treated to remove traces of contaminating chemicals and DNA, respectively, using RNeasy Mini kit (QIAGEN). Purified RNA samples were quantified using Qubit RNA Broad-range assay Kit (Thermo Fischer Scientific). Total RNA-seq libraries were prepared from 1 μg of purified RNA using the TruSeq Stranded Total RNA LT with Ribo-Zero (Human/Mouse/Rat, Set A) sample preparation kit (Illumina) according to the manufacturer's instructions. Libraries were pooled together and single-end sequenced with a read-length of 50 bp on an Illumina HiSeq1500 (Illumina). Approximately $3*10^7$ reads were generated per each multiplexed library.

For the expression profiling, read counts were generated for each of the RefSeq transcripts, using exon positions from UCSC hg19. RPKMs (reads per kilobase per million) were calculated

by normalizing read counts for each transcript by the transcript length and the total number of reads in the corresponding sample, and summed for each gene symbol. The RPKMs for the samples were then clustered using unsupervised, hierarchical clustering with a Ward distance measure. Counts per million (CPM) and differentially expressed transcripts were called using edgeR (51). Transcripts remained in the analysis if they had CPM>1 in all CK or control samples. The log2 fold change (logFC) and the false discovery rate (FDR) were then generated using the filtered group.

Gene expression profiles were clustered using the GeneE software, based on Pearson's correlation. Gene ontology (GO) analysis was performed using the PANTHER database (www.panther.org). Enriched GO terms with at least five represented genes and p<0.05 were included in the analysis.

45.   Gibbard CR, et al. (2013) White matter microstructure correlates with autism trait severity in a combined clinical-control sample of high-functioning adults. *NeuroImage Clin* 3:106–114.

46.   Filippi CG, Uluğ AM, Deck MDF, Zimmerman RD, Heier LA (2002) Developmental delay in children: Assessment with proton MR spectroscopy. *Am J Neuroradiol* 23(5):882–888.

47.   Komoroski RA, et al. (2004) Brain metabolite concentration ratios in vivo: Multisite reproducibility by single-voxel1H MR spectroscopy. *Magn Reson Imaging* 22(5):721–725.

48.   Ozturk A, et al. (2009) Proton MR spectroscopy correlates of frontal lobe function in healthy children. *Am J Neuroradiol* 30(7):1308–1314.

49.   Safriel Y, Pol-Rodriguez MA, Novotny EJ, Rothman DL, Fulbright RK (2005) Reference values for long echo time MR spectroscopy in healthy adults. *Am J Neuroradiol* 26(6):1439–1445.

50.   Staffen W (2005) Magnetic Resonance Spectroscopy of Memory and Frontal Brain Region in Early Multiple Sclerosis. *J Neuropsychiatr* 17(3):357–363.

51.   Robinson MD, McCarthy DJ, Smyth GK (2009) edgeR: A Bioconductor package for differential expression analysis of digital gene expression data. *Bioinformatics* 26(1):139–140.

Figure legends

Figure 1: *THRA* mutations are associated with structural abnormalities in brain

(A) Structural modelling of the ligand binding domain of TRα1 showing the position of mutations (red). The mutations in patients (P4: A382PfsX7; P2, P3: F397fs406X; P1:E403X) disrupt or truncate the carboxyterminal alpha helix (H12, black) of receptor, exposing a hydrophobic cleft that facilitates corepressor (CoR, blue) binding by unliganded receptor (left) and removing or changing aminoacids required for T3 (cyan) binding and coactivator (green) recruitment (right).

(B) MRI scans of patients (P1 to P4), with T2-weighted axial images (top row) and T1-weighted coronal images (bottom row), showing increased CSF space around cerebellum and between folia denoting reduced cerebellar size.

(C) Sagittal images from MRI brain scans of adult cases (P3, P4) showing microencephaly.

(D) Tract-based spatial statistics analysis of diffusion tensor imaging data in patients (P1, P2). Tracts highlighted in blue signify greater mean diffusivity (MD) of water than in controls (n=20 age and gender-matched subjects) and tracts highlighted in green denote not significantly different MD to controls.

Figure 2: Inefficient cortical induction of *THRA* mutation-containing iPSCs

(A) Schematic of the *in vitro* cortical differentiation protocol.

(B) TRα1 is expressed in cycling Ki67$^+$ progenitors as well as postmitotic Tuj1$^+$ neurons derived from control iPSCs. Scale bars, 50 μm.

(C) Representative pictures showing reduced progenitor rosette formation and Pax6 expression in control and *THRA* mutation-containing cells at day 15. Scale bars, 50 μm.

Supplementary Figure 1: *THRA* mutation-containing iPSCs can be induced to neural fate with variable efficiency

(A) Patient-derived iPSCs expressed the transcription factors Nanog, Oct4 and Sox2, as well as the membrane proteins TRA-1-60 and SSEA4, which are characteristic markers of pluripotent cells (23). The neural stem cell marker Nestin was not expressed. Scale bars, 100 μm.

(B) RT-PCR confirmed expression of Foxg1 and Pax6 in *THRA* mutation-containing and control cells (H9, NDC, NAS9) . –RT, no transcriptase.

(C) Pax6 expression is variable in TRα1 mutation-containing cells at D12. Scale bars, 50 μm.

(D) Western blot analysis confirms TRα1 expression in control cells at D50 and D80 (green, β-actin; red, TRα1).

Figure 3: RNA-seq reveals downregulation of transcription, neurogenesis, and cell-cell adhesion in *THRA* mutation-containing cells

(A) Two-dimensional hierarchical clustering of $\log_2$(RPKM) values for three inductions each from control iPSCs and the three patient lines. Colours correspond to relative expression in each row, from lowest (blue) to highest (red). Inductions cluster by cell line of origin (vertical axis), while genes separate into four differentially expressed groups (horizontal axis).

(B) FDR q-values of GO terms enriched among group C genes.

(C) Gene ontology analysis reveals that genes implicated in nervous system development that are downregulated in *THRA* mutation-containing cells partially overlap with cell-cell adhesion genes (8/42, 19%) and DNA-templated transcription (10/42, 24%).

Figure 4: FACS-enriched *THRA* mutation-containing cortical progenitor cells generate functional neuronal networks

(A) Representative FACS results for WT and *THRA* mutation-containing cells at day 18. Immunocytochemistry confirmed the cortical identity of FACS selected progenitor cells. Scale bars, 50 μm.

(B) Neurons produced by FACS-purified progenitor cells expressed the cortical layer-specific transcription factors TBR1 (layer VI) and CTIP2 (layer V), as well as the vesicular glutamate transporter vGlut1, at day 40. Scale bars, 50 μm.

(C) Representative traces showing action potential firing in response to stepwise current injection in *THRA* mutation-containing and control neurons. Numbers indicate the proportion of cells that fired action potentials.

(D) Calcium indicator Oregon Green BAPTA was used as a proxy for action potential firing to measure spontaneous neuronal activity. Fluorescence images show control and *THRA* mutant cultures after loading. Heat maps highlighting different levels of activity across the cultures. Total calcium activity across the field of view, A_{Ca}, was quantified based on 2-3 independent experiments for each iPSC line (Methods). Error bars indicate SEM.

Supplementary Figure 2: *THRA* mutation-containing neurons show normal electrophysiological properties and spontaneous excitatory synaptic neurotransmission

(A) Top row, representative traces showing sodium and potassium currents in response to voltage stimulation in *THRA* mutation-containing and control neurons, and quantification of the mean peak sodium current (FS397, n=14; control, n=14). * p<0.05 (Student's t-test). Bottom row, representative traces recorded in voltage clamp mode from *THRA* mutation-

containing and control neurons held at -70 mV, and quantification of the proportion of cells that showed spontaneous activity (FS397, n=14; control, n=14).

(B) Calcium indicator Oregon Green BAPTA was used as a proxy for action potential firing to measure spontaneous neuronal activity (see Figure 3D). Representative traces show the time course of the fluorescent signal (ΔF/F) observed in the ten most active cells in the field of view.

(C) Representative calcium imaging traces of *THRA* mutation-containing and control cells at day 50 before and after treatment with the sodium channel blocker tetrodotoxin (TTX) or the AMPA receptor antagonist CNQX. Spontaneous activity returned after washout (traces following washout of CNQX looked equivalent).

Figure 5: Clonal lineage analysis reveals marked differences between *THRA* mutation-containing and control progenitor cell dynamics

(A) Schematic of the experimental protocol. GFP-labelled cortical progenitor cells were enriched for by FACS and mixed with WT cultures at day 30 or 40. Cultures were fixed for analysis after 2, 6 or 10 days of incubation.

(B) Representative images of *THRA* mutant and control clones derived from a single progenitor cell after 2, 6 and 10 days, immunostained for Ki67 (progenitors) and βIII-tubulin (neurons). Scale bars, 50 μm.

(C) Average clone size and average number of Ki67$^+$ cells per clone over time (each data point represents the average of n=50–72 clones). Error bars indicate SEM.

Supplementary Figure 3: Cell cycle time and cell death in *THRA* mutant and control cells

(A) Example of an apical division in which the apically anchored mother cell (green arrow) undergoes interkinetic nuclear migration and divides near the rosette centre, giving rise to two daughter cells (blue and yellow arrows) which also both retain apical processes.

(B) The distribution of cell cycle times of *THRA* mutant and control apical progenitors (n=7 for both).

(C) Average cell cycle time of *THRA* mutant and control apical progenitors. Cell cycle times were measured as the time interval between the apical divisions of a cell and its daughter cell with apical processes. Error bars indicate SEM. n.s., not significant (p>0.01, Student's t-test).

(D) Example of a live-imaged putative progenitor cell undergoing apoptosis.

(E) The fraction of cells that went through apoptosis over a period of 12 h. Neurons were distinguished from progenitor cells based on their characteristic morphology and location at the periphery or outside of rosettes. Error bars indicate SEM (n=100 cells were tracked for each measurement). n.s., not significant (p>0.01, Student's t-test).

Figure 6: Clonal dynamics are consistent with a simple model of reduced progenitor output in *THRA* mutants

(A) The frequency of clones consisting of only Ki67$^+$ cells (rose), only Ki67$^-$ cells (gray), or both (green), at the different time points (days post mixing, dpm). Scale bar, 50 μm.

(B) Average clone sizes of persisting clones, with model fit (green line), and average number of Ki67$^+$ cells with the model prediction using the best-fit parameters (red line).

(C) Total clone size distributions and model predictions (lines); each histogram represents n=152–176 clones.

In A and B, data points represent the average of three control and three *THRA* mutant lines; error bars indicate SEM.

Supplementary Figure 4: Clonal composition in control and *THRA* mutant cortical cells

(A) The size distribution of fully Ki67$^-$ clones at 6 and 10 days post mixing (dpm), and model fit. Data points represent the average of three control and three *THRA* mutant inductions; error bars indicate SEM.

(B) The joint distribution of Ki67$^+$ and Ki67$^-$ cells in *THRA* mutant and control clones at 2, 6 and 10 days post mixing at age 30 or 40 days. Colours indicate the fraction of clones at each coordinate. Results represent the average of three control and three *THRA* mutant lines.

Figure 7: Cortical rosette self-organised assembly is impaired in *THRA* mutant cultures

(A) Schematic of the experimental protocol. Dissociated NPCs were plated onto micropatterned chips containing fields of diameter 140 μm and cultured for several days.

(B) Phase contrast images of individual micropatterned fields at 24 h and 48 h after plating (Control-H9 cells). Scale bar, 100 μm.

(C) Immunostainings of rosettes fixed 48 h after plating (control cells). Since RGs *in vitro* are connected by adherens junctions (AJs) at their apical ends (22), expression of the AJ component N-cadherin (top left) was used to visualise rosette centres. Rosettes contained Ki67$^+$ cycling cells, and MAP2$^+$ neurons were frequently observed at the periphery (top right). The centrosome protein γ-tubulin and the apically expressed atypical protein kinase C

were localised to rosette centres (both bottom pictures), demonstrating the apical-basal polarity of Pax6$^+$ and Nestin$^+$ progenitor cells. Scale bars, 50 μm.

(D) Representative images of *THRA* mutant and control progenitors plated onto micropatterned chips. N-cadherin (red) was used to visualize rosette centres. Scale bars, 50 μm. The bar chart summarizes the proportion of fields of diameter 140 μm that were occupied one rosette (72 to 405 fields from two independent inductions were considered for each line). * p<0.01 (Student's t-test).

Supplementary Figure 5: A minimal model for rosette formation *in vitro*

(A) Control cultures (NDC) dissociated at day 25 and treated with 10 μM 1-850 or DMSO (control) for five days. Treatment with 1-850 reduced the number of rosettes per field of view, which were identified as radially arranged nuclei around foci of atypical protein kinase C (yellow circles). The proportion of cycling cells was also reduced. Scale bars, 100 μm. * p<0.05, ** p<0.01 (Student's t-test).

(B) Dissociated *THRA* mutant (P1) and control (NDC) cultures were plated onto micropatterned chips and live imaged for a period of 48 hours, starting at 24 hours after plating. Shown are 10 representative traces of cellular movement, with no evidence for directionality. *THRA* mutant progenitors exhibited slightly higher average migration speeds than controls, which may be the result of beginning rosette assembly in control cultures constraining movement.

(C) Rosette formation was reproduced by a simple computational model in which cells – approximated as rods of length 20 μm – undergo random movement at a speed of 17 μm per frame (10 min) in two dimensions, and attach to each other at their apical ends when within 17 μm. Once formed, attachments are assumed to persist indefinitely. Over time, this dynamic leads to rosette formation *in silico* (top; purple dots represent the apical ends of cells, and black dots represent two or more apical ends that have attached to each other). The number of rosettes and the distribution of rosette centres observed *in vivo* are statistically reproduced by the model (bottom; NDC, n=50; simulation, n=100).

(D) In control cultures, N-cadherin, γ-tubulin and PKCζ and were localised to the apical end of progenitor cells in rosettes. In THRA mutants, expression of these factors was diffuse or greatly reduced. Scale bars, 50 μm.
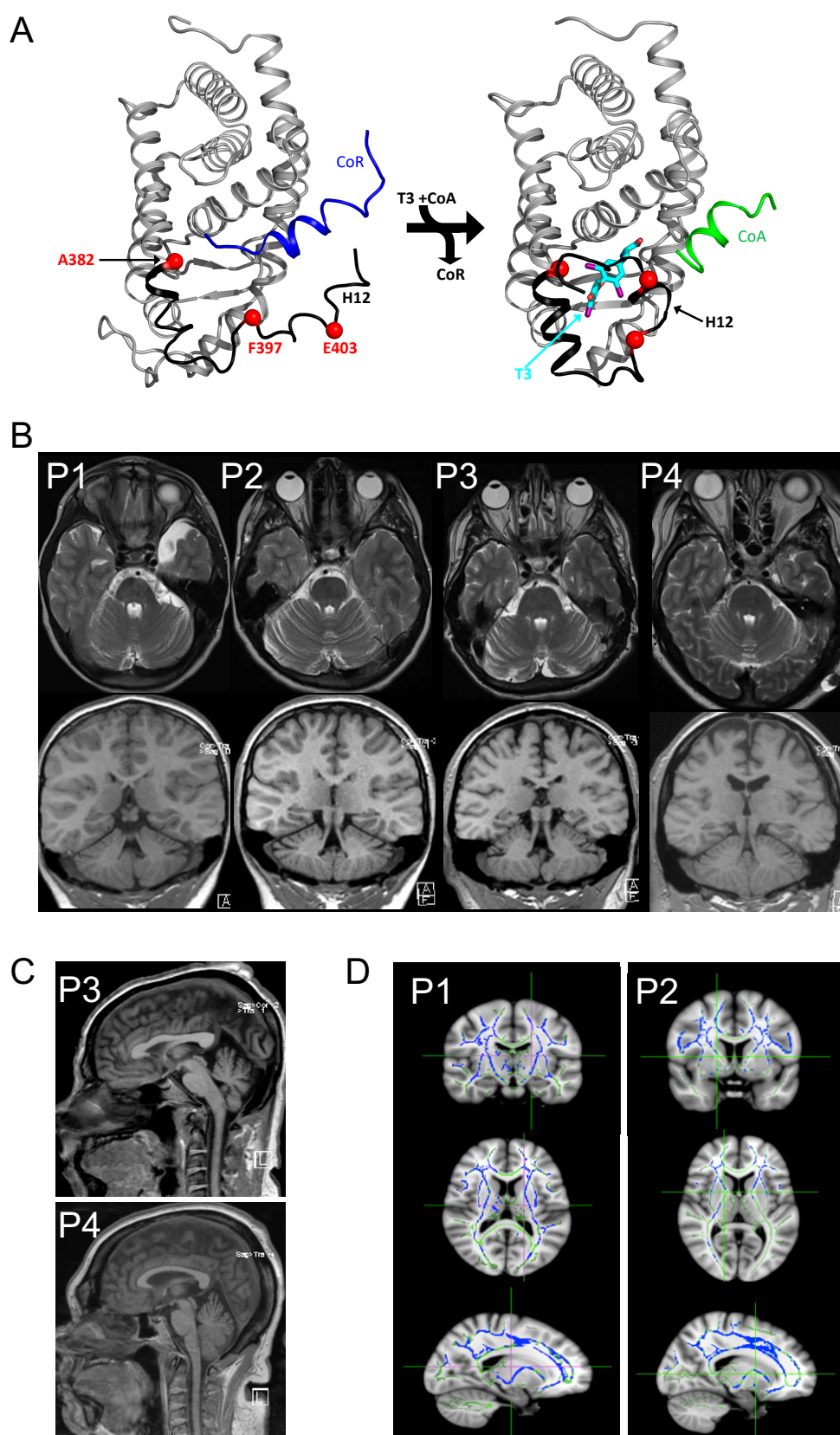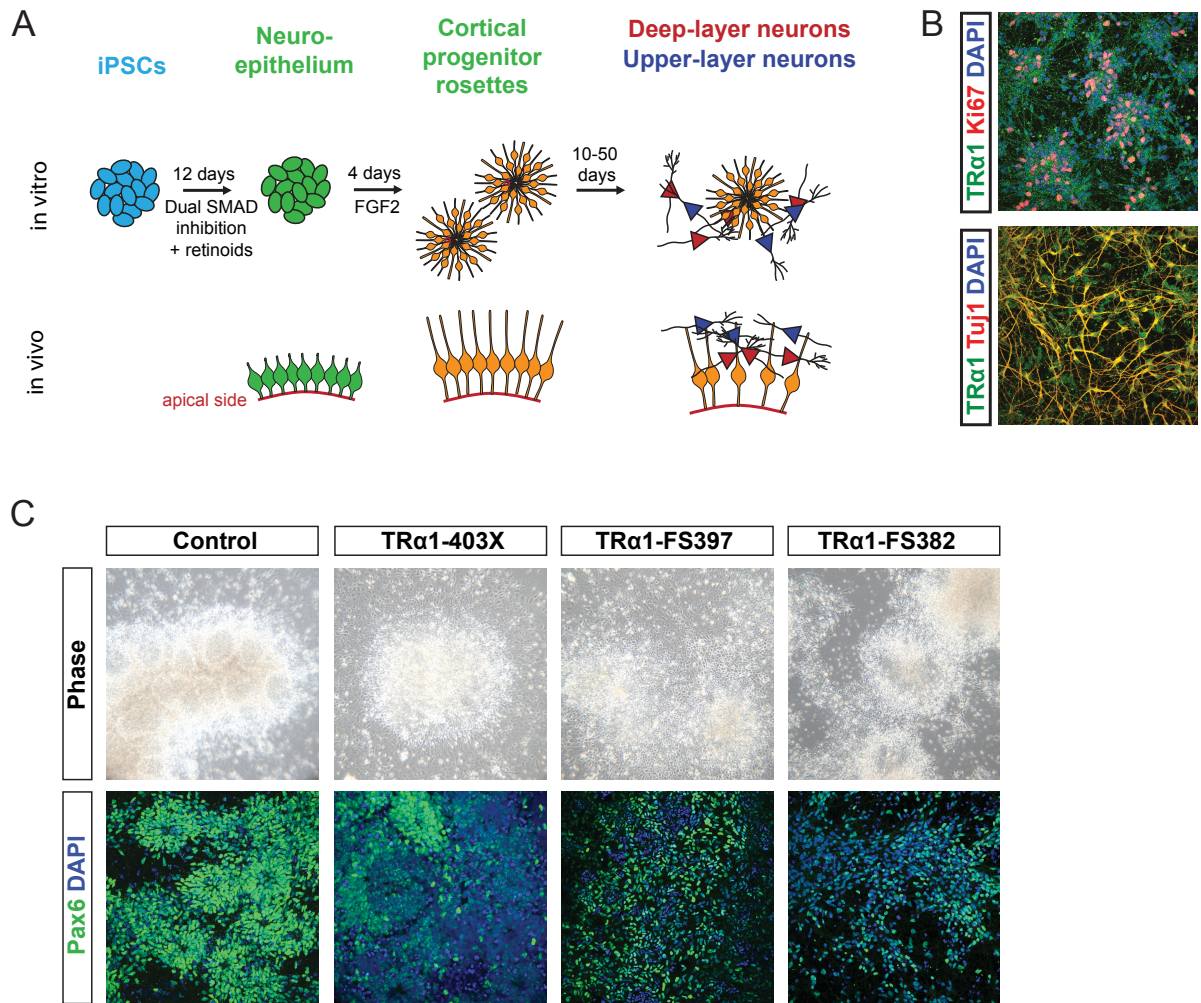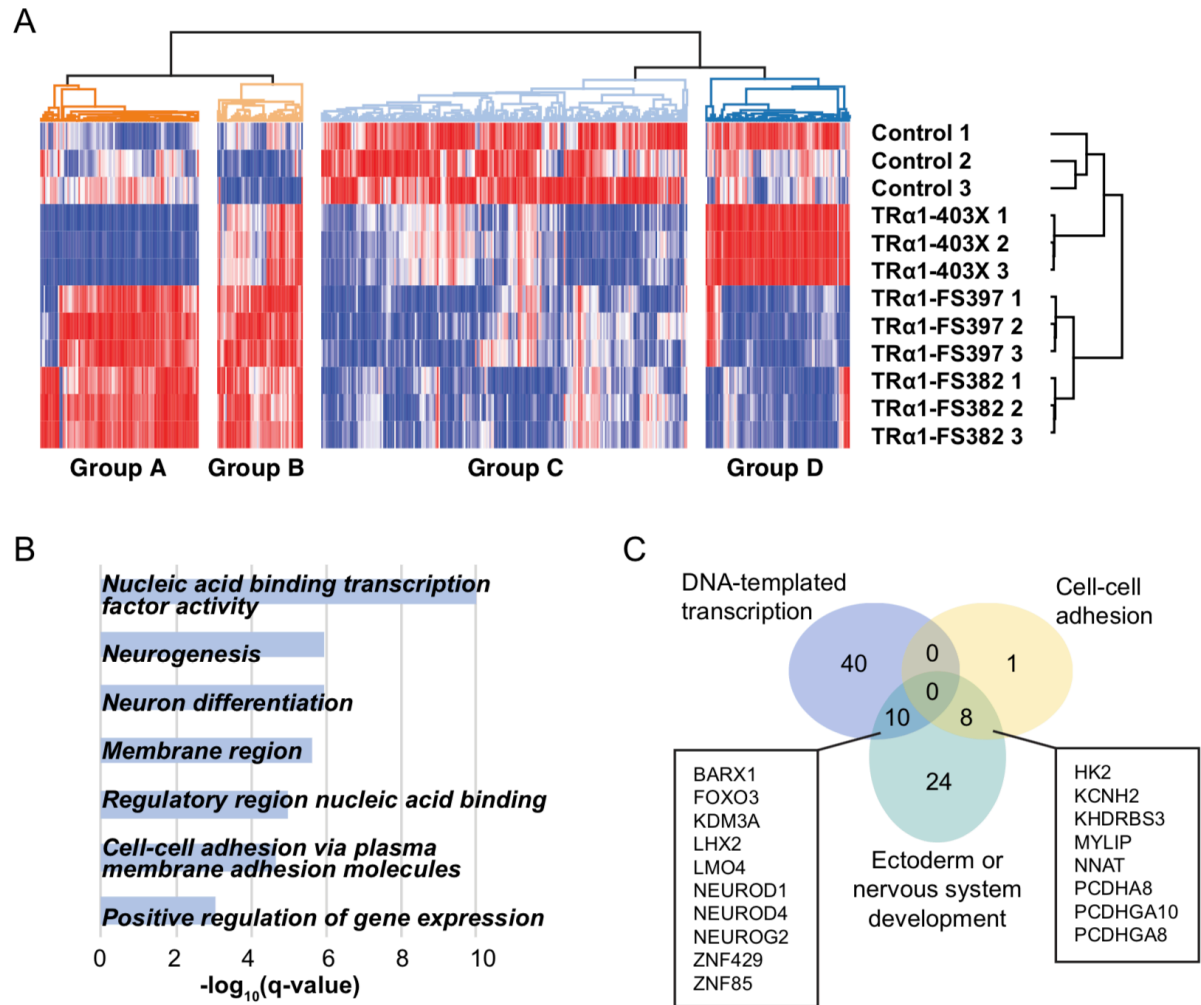
Figures

Figure 1:

Figure 2:

Figure 3:

Figure 4:
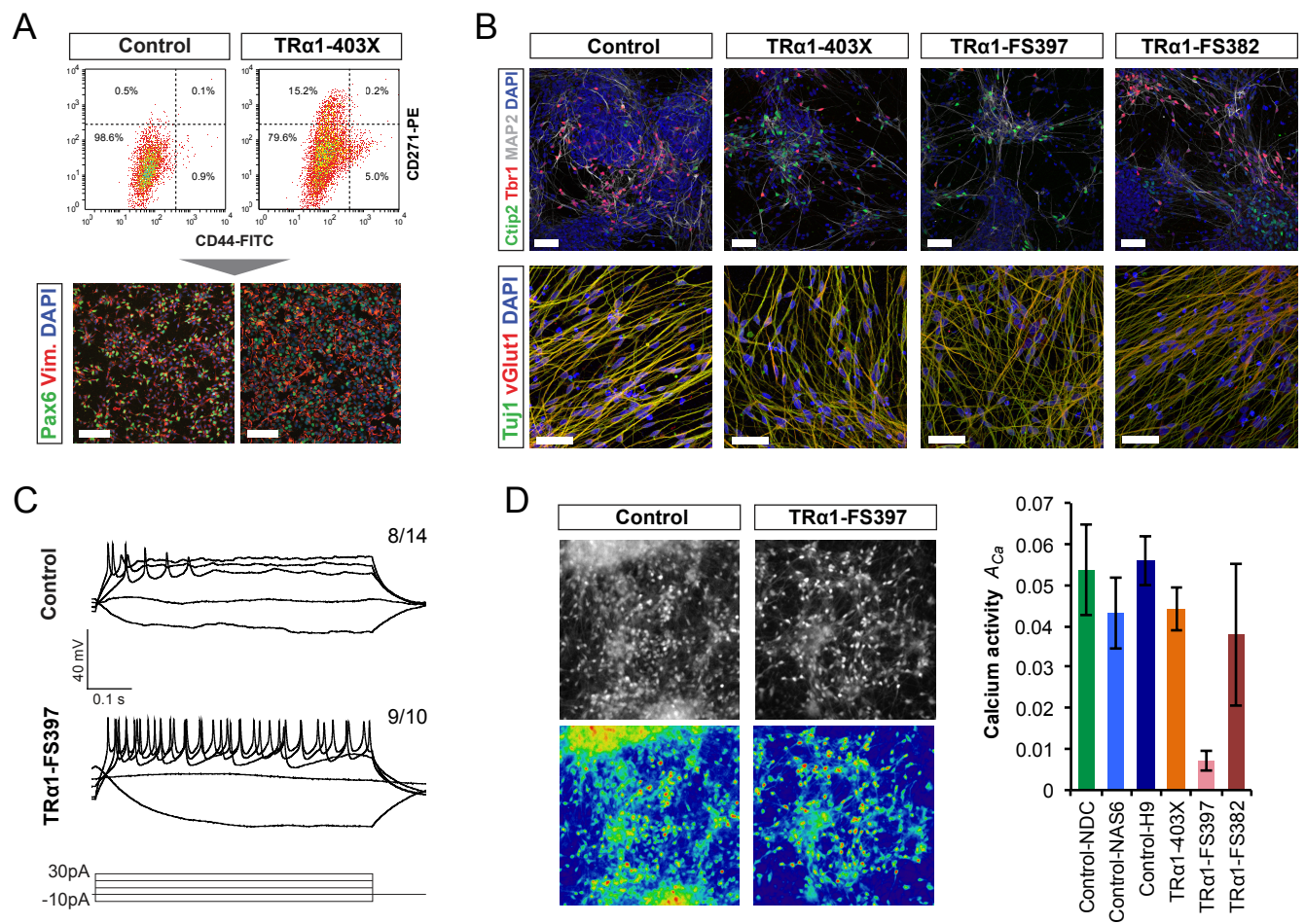
Figure 5:

Figure 6:

Figure 7:

acetylated α-tubulin N-cadherin DAPI
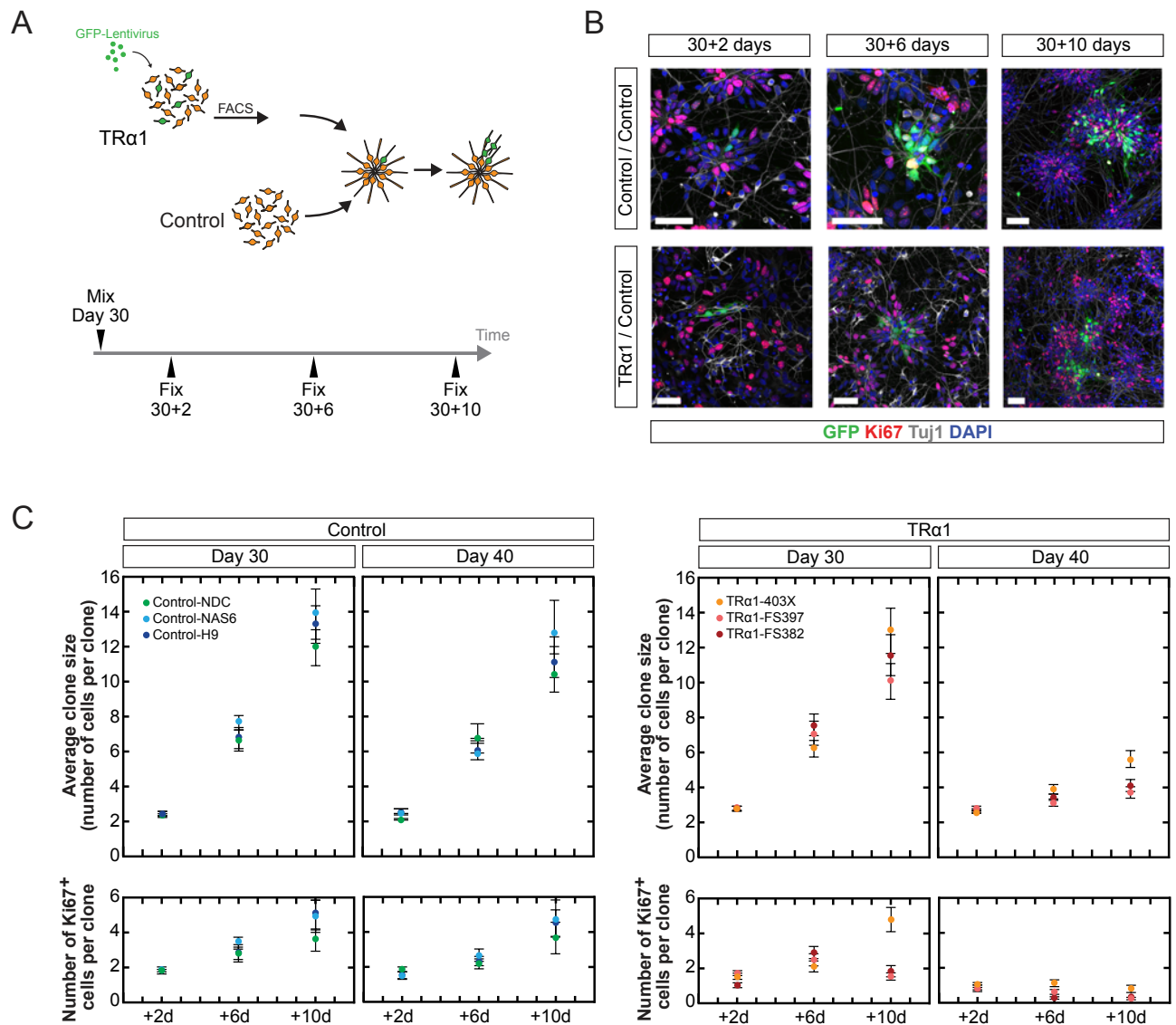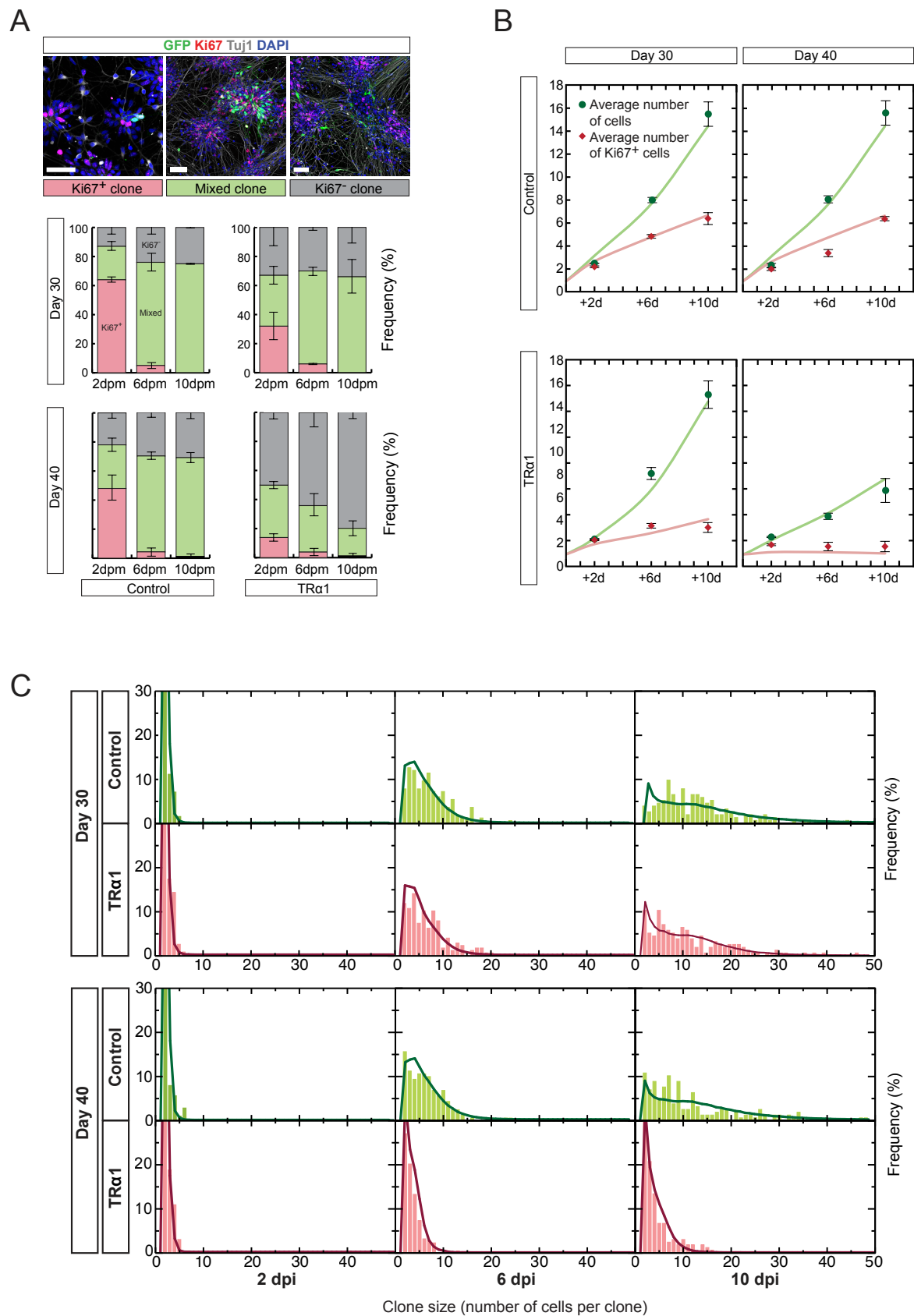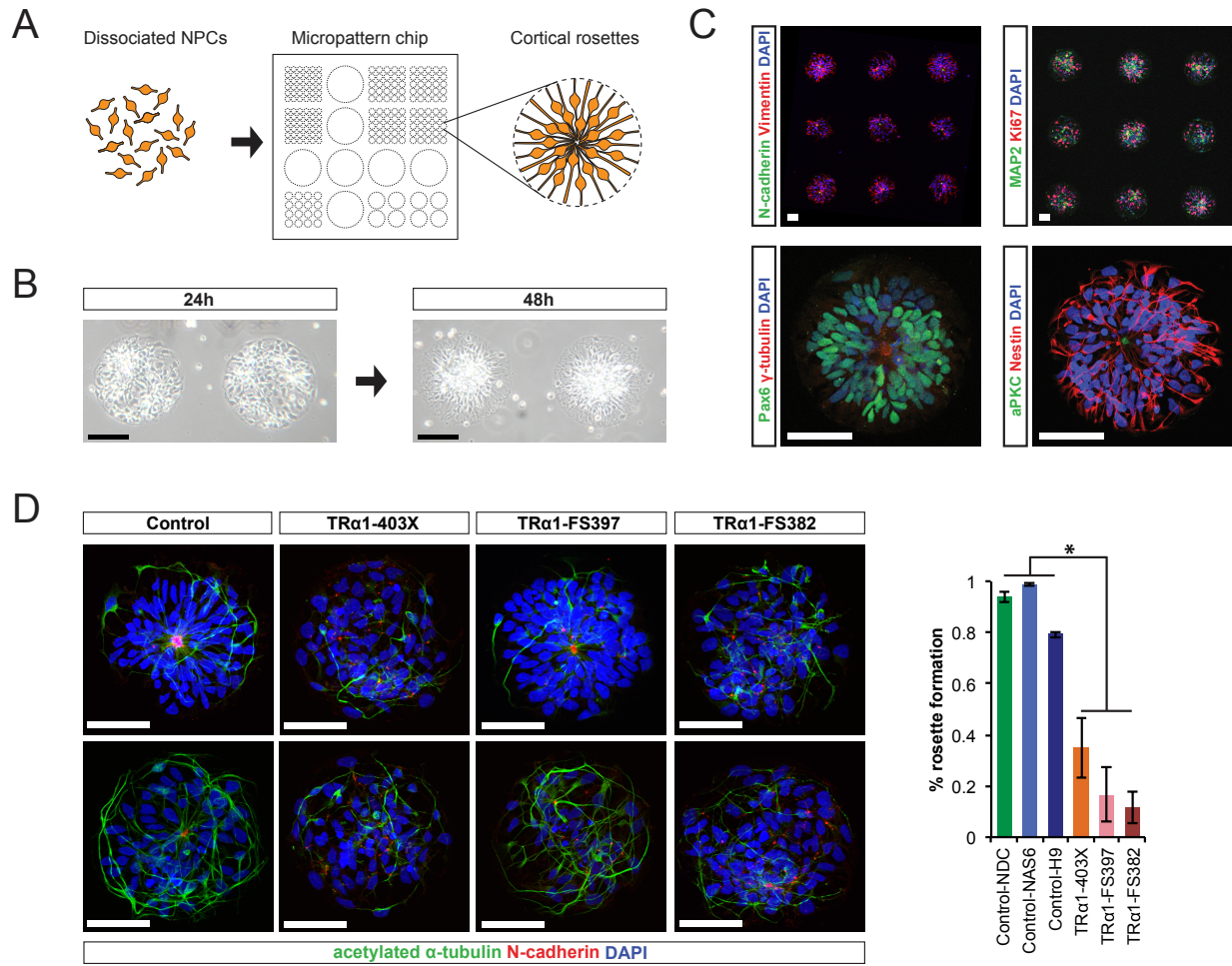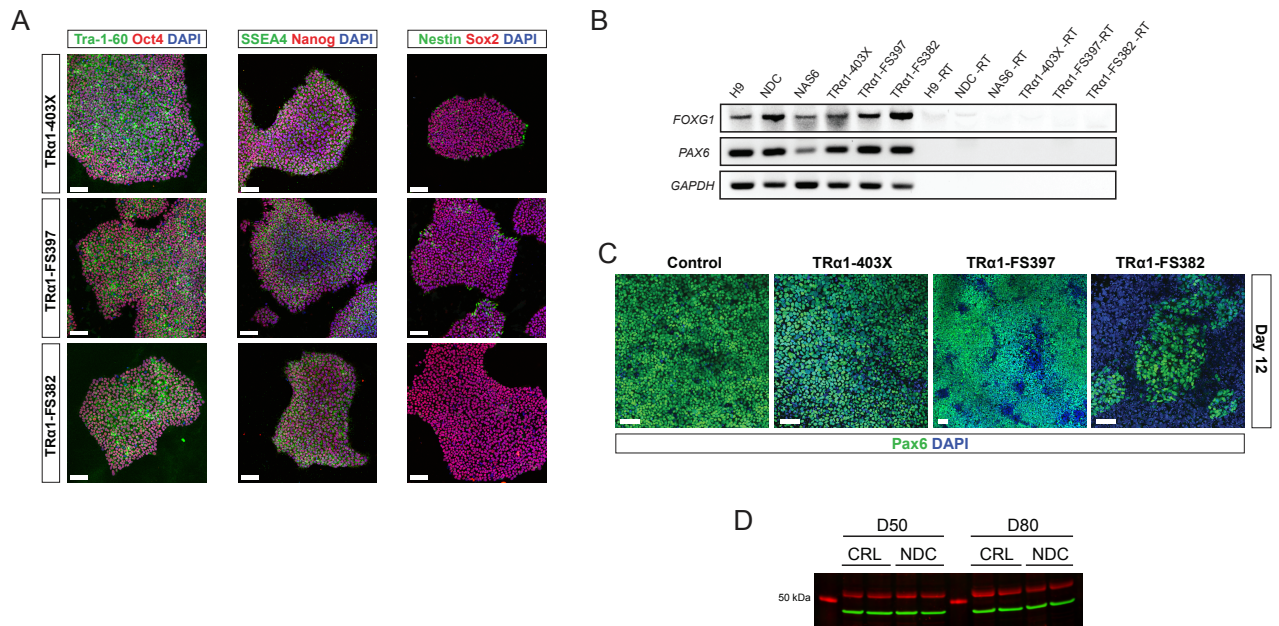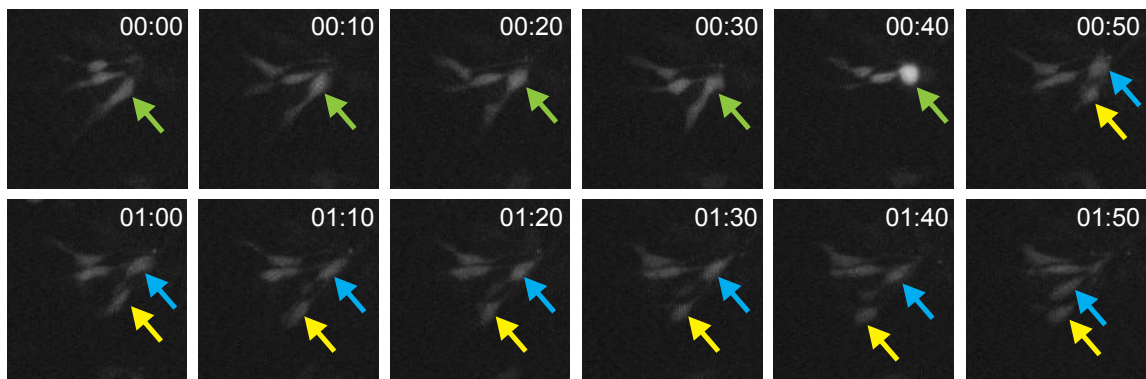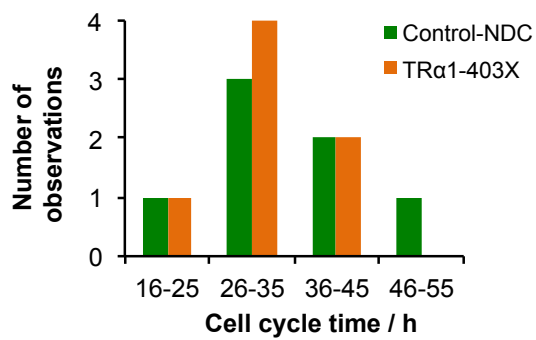
Supplementary Figures

Supplementary Figure 1:
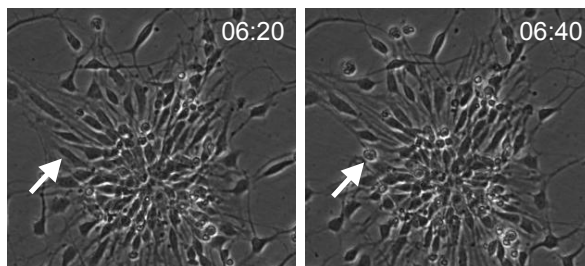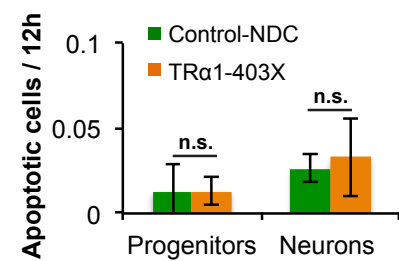
Supplementary Figure 2:
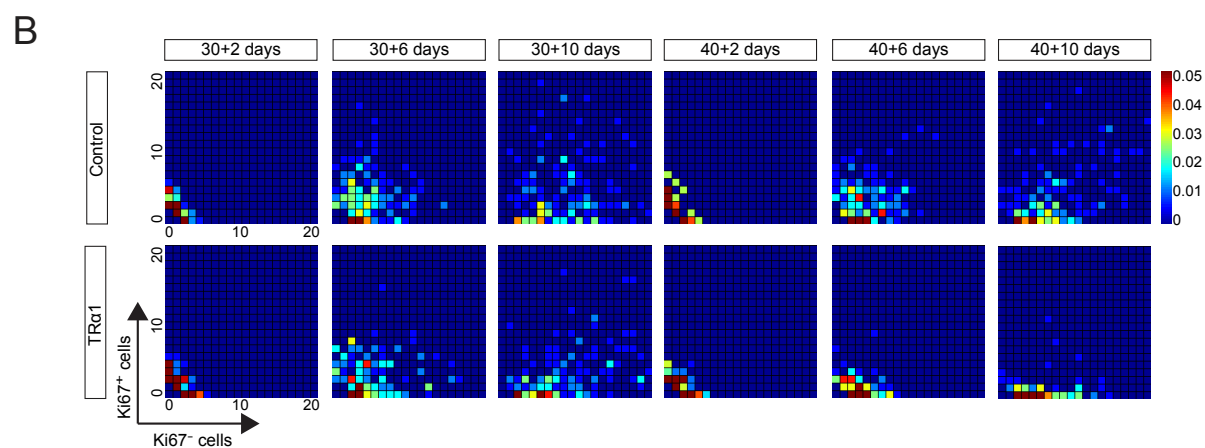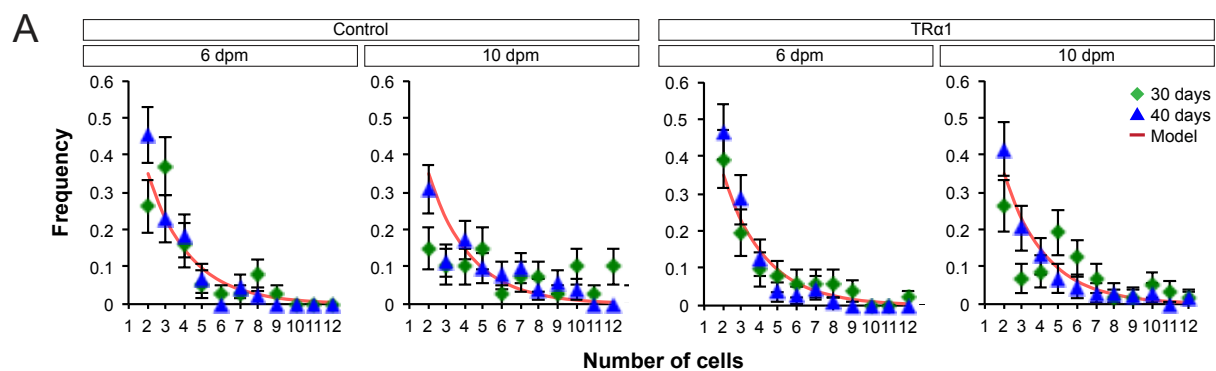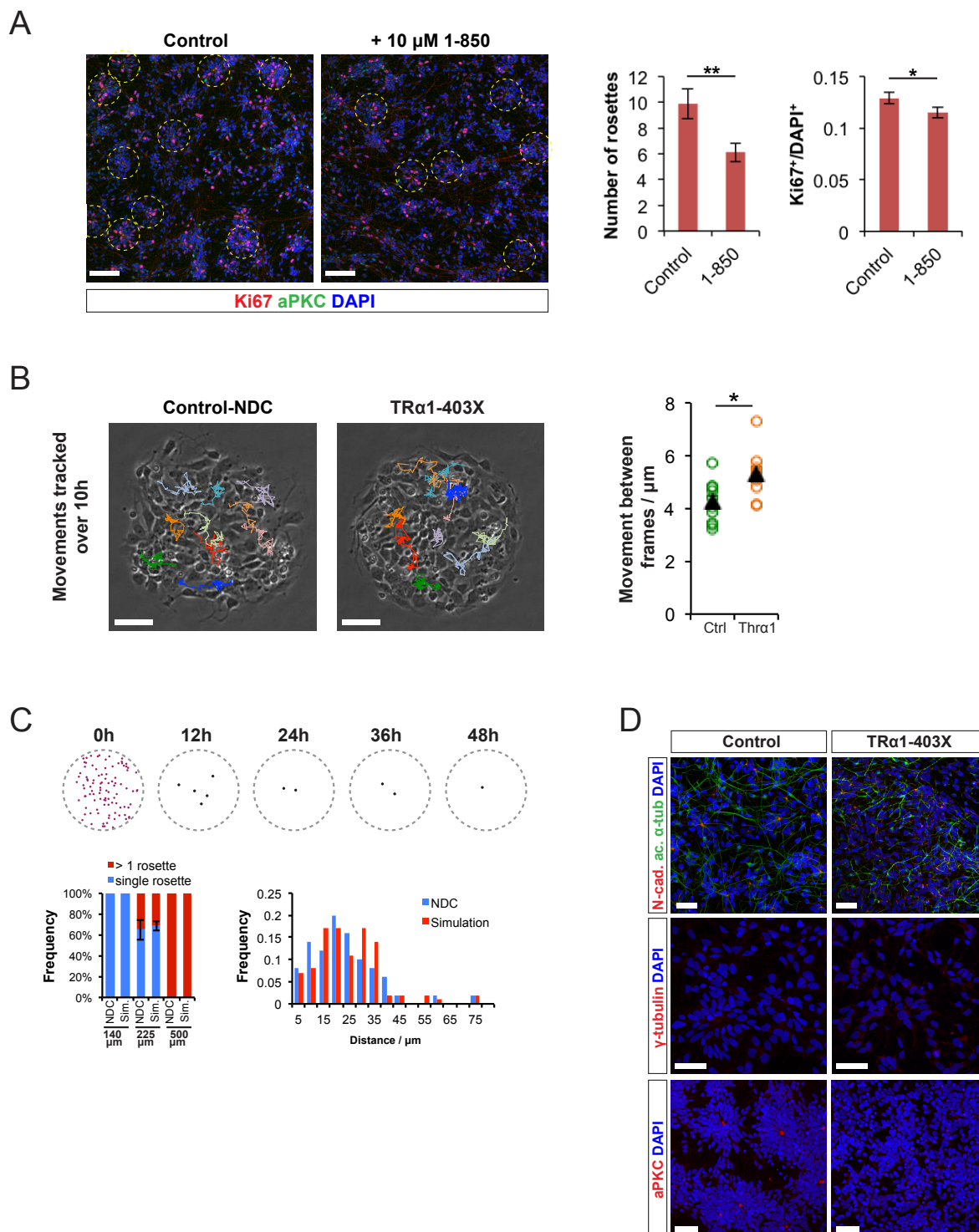
Supplementary Figure 3:
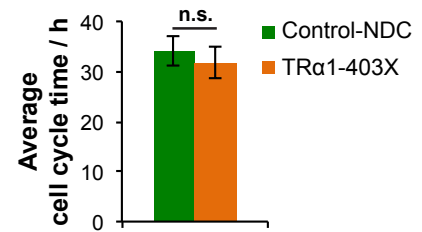
Supplementary Figure 4:

Supplementary Figure 5:

Supplementary Tables

Table 1: Characteristics of RTHα patients who underwent neurocognitive and neuroimaging assessment

	P1	**P2**	**P3**	**P4**
THRA Mutation	E403X	F397fs406X	F397fs406X	A382PfsX7
Age at Diagnosis	6 years	12 years	47 years	48 years
Age at phenotyping	8.5 years	13.5 years	47 years	49.5 years
Gender	Female	Female	Male	Female

Table 2: Summary of neurological findings in patients

	P1	P2	P3	P4
Slow to initiate movement	++	+	+	+++
Abnormal Gait (broad based, ataxic)	+	+	+	+++
Abnormal Speech (slow, dysarthric, thick quality)	++	+	+	+++
Dysdiadochokinesis	+	+	+	+
Intention tremor	-	-	-	+
Slow Relaxing reflexes	+	+	-	-
Fine and Gross Motor incoordination	++	+	-	+++
Hypotonia	+	-	-	-

+++ severe, ++ moderate, + mild.

Table 3: Summary of developmental milestones in patients

	P1			P2	P4
	Age 16 months	Age 20 months	Age 27 months		
Gross Motor Skills	7-9 months	12-13 months	15-18 months	Sit 9 months, walk 19 months	Walking at 4 years
Fine Motor Skills	13-18 months	18-21 months	24 months		"poor"
Communication	11-15 months	11-18 months	11-18 months	First words 19-20 months, short sentences 2-4 years	First spoke at 3.5 years

No developmental data are available for P3.

Table 4: Summary of neuropsychological parameters in patients

Test Domain	P1	P2	P3	P4
* Nonverbal IQ	Low	Low	Low	Exceptionally Low
+ Visual Perception	Average	Low Average	Average	Exceptionally Low
+ Visual Motor Integration	Low	Low	Exceptionally Low	Exceptionally Low
+ Motor Coordination	Exceptionally Low	Exceptionally Low	Exceptionally Low	Exceptionally Low
§ Finger Dexterity Dominant Hand	Exceptionally Low	Exceptionally Low	Exceptionally Low	----
§ Finger Dexterity Non-Dominant Hand	Exceptionally Low	Exceptionally Low	Exceptionally Low	----

* Wechsler scales (P1 and P2 WISC-IV, P3 WAIS-IV, P4 WASI-II)
+ Beery-Buktenica Developmental Test of Visual Motor Integration Sixth Edition
§ Annett Peg Sorting Test

Table 5: N-Acetylaspartate/Total Creatine (NAA/Cr) ratio measured by MRS

	P2	P3	P4	Range of Control Values
Frontal White Matter	1.77	1.57	1.54	2.19-2.5
Thalamus	1.91	2.06	1.94	2.09-2.24

Supplementary Methods

Computational model of human cerebral cortex neurogenesis

The modeling scheme used to analyse the clonal lineage data was based on the findings of a recent *in vivo* genetic labeling study of cortical neurogenesis in mouse, which showed that cortical radial glia progenitor cells (RGs) transit from a symmetrical proliferative phase to a neurogenic phase, in which they asymmetrically give rise to intermediate progenitor cells (IPCs) with variable but limited neurogenic potential (52). In primates, the progenitor cell compartment is more complex, including ventricular and outer radial glia that interconvert between different subtypes (53, 54). While a comprehensive quantitative description of human cortical development was thus not feasible, this analysis aimed to identify robust differences in progenitor cell dynamics between Thrα1 mutant and control cell lines. We considered the evolution of clones in control lines first and, in a second step, compared these findings to the Thrα1 mutant clonal data.

Clonal behaviour in control cultures

As RGs are defined by their long-term self-renewal potential, clones that have lost all Ki67$^+$ cells by 10 days post-mixing (dpm) are assumed to derive from IPCs. The distribution of Ki67$^-$ clones was consistent with a model in which IPCs cycle at a constant rate λ_I and, on each division, self-renew asymmetrically with probability q, or differentiate symmetrically with probability $1-q$. The distribution of cell cycle times was approximated as a Gamma distribution with scale parameter $\theta_I = 0.5$; within a reasonable range, the exact choice of scale parameter proved inconsequential. The size distribution of Ki67$^-$ clones labelled at day (D) 30 and D40 in control lines was then well approximated with $q = 0.65 \pm 0.05$ and $\lambda_I = 0.65 \pm 0.05$ per day, consistent with IPC behaviour remaining constant over the time period considered here (Supplementary Fig. 4A). As expected, by 10 dpm, this model predicts that all IPC-derived clones are fully differentiated. From the fraction of Ki67$^-$ clones at 10 dpm (see Fig. 6A), and assuming that RGs and IPCs are labelled with equal efficiency, it followed that around 25% of cycling cells at day 30, and 31% at day 40, are IPCs.

In mouse neocortical development, RGs transition through a series of symmetric proliferative divisions before entering a phase of asymmetric divisions into IPCs or neurons (52). To determine whether a similar sequence of events could be distinguished in the human data, we considered the joint distribution of Ki67$^-$ cells, which are mostly or exclusively neurons, and Ki67$^+$ cells, which include RGs and IPCs, in clones (Supplementary Fig. 4B). In the D30 data at 6 dpm, some clones contained up to seven Ki67$^+$ and no differentiated cells, indicating that at least a proportion of cycling cells are still proliferating symmetrically. By 10 dpm, however, no clones were observed that consisted of more than seven Ki67$^+$ cells but no neurons. Therefore, progenitors that initially divided symmetrically are producing neurons by 10 dpm.

At the same time, a similar frequency of seven-cell Ki67^{+}-only clones was also observed at 10 dpm in the day 40 data. Given the asymmetric division pattern of IPCs, this suggests that RGs do not transition unidirectionally from symmetric to asymmetric divisions.

Instead, we probed whether their dynamics were consistent with a model in which the choice between symmetric and asymmetric divisions is made stochastically at the level of individual RGs. In this model, RGs cycle at a constant rate λ_R and, on each division, self-renew symmetrically with probability r_{PP}, asymmetrically produce an IPC with probability r_{PD}, or produce two IPCs with probability 1-r_{PP}-r_{PD}. Again, the cell cycle times were taken to follow a Gamma distribution. Since the scale parameter, θ_R, significantly affected the outcome in this case, it was included as a parameter to fit.

Fitting the model by weighted least squares to the observed average sizes of 'persisting' clones, meaning clones that retain at least one Ki67^{+} cell, good accordance was achieved for the D30 control data with $\lambda_R = 0.47 \pm 0.02$ per day, $r_{PP}= 0.30 \pm 0.05$, $r_{PD}= 0.65 \pm 0.05$, and $\theta_R = 1.1 \pm 0.3$ (Fig. 6B). Importantly, with these parameters, the model predicts the size distribution of 'persisting' clones at 6 dpm and 10 dpm. The total clone size distribution, including fully differentiated clones, was also well predicted (Fig. 6C).

The same parameter choice resulted in a good approximation of the clonal data from control cultures infected with GFP-lentivirus at day 40 (Fig. 6B,C), suggesting that any change in progenitor cell behaviour over this time period is small.

Clonal behaviour in TRα1 mutant cultures

The distribution of Ki67^{-} clones in TRα1 cultures was indistinguishable from control cultures, suggesting that IPC behaviour is not affected by TRα1 mutations (Supplementary Fig. 4A). However, the fraction of fully differentiated clones in the D30 data was higher than in controls; only 66% of clones retained Ki67^{+} cells at 10 dpm (see Fig. 6A). Assuming, as before, that these persisting clones are derived from RGs, the fitting procedure was repeated for the TRα1 mutant data at D30, using the cell cycle parameters λ_R and θ_R found from the control lines. A good approximation of the average 'persisting' clone sizes was obtained with $r_{PP}= 0.15 \pm 0.03$ and $r_{PD}= 0.80 \pm 0.05$ (Fig. 6B). With these parameters, the model correctly predicts the size distribution of 'persisting' clones and consequently the total clone size distribution (Fig. 6C).

In the D40 clonal data, only 20% of clones contained cycling cells at 10 dpm, and the average clone sizes were markedly decreased (Fig. 6A,B). With $r_{PP}= 0.05 \pm 0.05$ and $r_{PD}= 0.10 \pm 0.05$, the average clone sizes were still well approximated (Fig. 6B); a satisfactory approximation of the clone size distribution was also obtained (Fig. 6C). The fate choice probabilities r_{PP} and r_{PD} are therefore significantly reduced in TRα1 mutant compared to control cultures at D40.

Premature neurogenesis and progenitor depletion

To summarise, the control clonal data at D30 and D40 are well approximated by a highly simplified model of cortical development. In this model, RGs cycle on average once every 51 ± 2 hours. On each division, they choose stochastically between symmetric self-renewal with a probability of 30 ± 5 %, asymmetric division with a probability of 65 ± 5 %, or symmetric differentiation into IPCs. IPCs themselves cycle on average once every 37 ± 3 hours. 65 ± 5 % of IPC divisions are asymmetric and the remainder are symmetric differentiating divisions into two neurons, which results in virtually all IPC-derived clones differentiating fully by 10 dpm. The TRα1 mutant clonal data is well described by the same model with the same cell cycle parameters, suggesting that the unidirectional lineage hierarchy (RGs producing IPCs which in turn give rise to Ns) and characteristic cellular properties are not affected by the mutations. Instead, the observed clone sizes and compositions are consistent with a change in RG fate choices upon division. At D30, the probability of symmetric self-renewal of RGs is only 15 ± 3 %, while 80 ± 5 % of divisions are asymmetric. At D40, the vast majority of divisions are symmetric differentiating divisions into two IPCs. Consistently, the estimated proportion of RGs in cultures decreases much faster in TRα1 mutant lines, reaching 20% at day 40.

The cell cycle times estimated from the clonal data agree well with earlier *in vitro* estimates based on clone sizes at 2 dpm and BrdU incorporation, as well as previously reported results from non-human primates (55). As a further consistency check, dissecting out the Ki67$^+$ cell content of clones, the model provides an independent prediction of the progenitor cell number within clones (see Fig. 6B).

While a more complex model might provide an equally good, or better, description of the data, these results suggest that the simplistic model introduced here contains the minimal necessary rules governing stem cell dynamics in TRα1 mutant and control cortical cultures. Importantly, the dramatic difference in clonal dynamics is largely accounted for by the premature differentiation of RGs into IPCs, without any changes to cell cycle kinetics or lineage hierarchy. Over time, the decreased self-renewal of RGs leads to a markedly different output predicted per initially labelled RG over the 20-day period from day 30 to day 50. In control cultures, on average, the model predicts that one RG labelled at day 30 gives rise to approximately 8.2 RGs, 8.1 IPCs, and 52.2 neurons by day 50. In stark contrast, in TRα1mutant cultures, the average RG labelled at day 30 results in less than 0.1 RGs, 1.2 IPCs, and 28.1 neurons over the same time period. Not only are neurons generated prematurely by TRα1 mutant progenitor cells, but the pool of RGs with long-term self-renewal potential is also depleted much earlier than in controls, leading to a reduction in the overall number of neurons produced during cortical development.

52. Gao P, et al. (2014) Deterministic progenitor behavior and unitary production of neurons in the neocortex. *Cell* 159(4):775–788.

53. Hansen D V, Lui JH, Parker PRL, Kriegstein AR (2010) Neurogenic radial glia in the outer subventricular zone of human neocortex. *Nature* 464(7288):554–561.

54. Betizeau M, et al. (2013) Precursor diversity and complexity of lineage relationships in the outer subventricular zone of the primate. *Neuron* 80(2):442–57.

55. Otani T, Marchetto MC, Gage FH, Simons BD, Livesey FJ (2016) 2D and 3D Stem Cell Models of Primate Cortical Development Identify Species-Specific Differences in Progenitor Behavior Contributing to Brain Size. *Cell Stem Cell* 18(4):467–480.